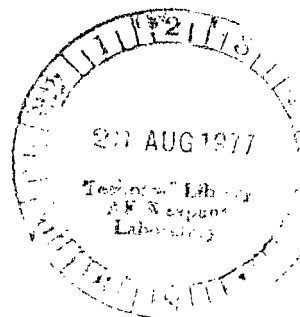# NASA TECHNICAL NOTE

NASA TN D-8468 *c.1*

ANALYSIS AND RADIANT HEATING TESTS
OF A HEAT-PIPE-COOLED LEADING EDGE

Charles J. Camarda

Langley Research Center
Hampton, Va. 23665

1. Report No. NASA TN D-8468	2. Government Accession No.	3. Recipient's Catalog No.
4. Title and Subtitle ANALYSIS AND RADIANT HEATING TESTS OF A HEAT-PIPE-COOLED LEADING EDGE		5. Report Date August 1977
		6. Performing Organization Code
7. Author(s) Charles J. Camarda		8. Performing Organization Report No. L-11247
9. Performing Organization Name and Address NASA Langley Research Center Hampton, VA 23665		10. Work Unit No. 505-02-12-01
		11. Contract or Grant No.
12. Sponsoring Agency Name and Address National Aeronautics and Space Administration Washington, DC 20546		13. Type of Report and Period Covered Technical Note
		14. Sponsoring Agency Code

15. Supplementary Notes

16. Abstract

The performance of a heat-pipe-cooled leading edge was investigated experimentally and analytically. The test model and radiant heaters were positioned to simulate aerodynamic heating distributions and gravity effects at angles of attack of 0°, 10°, and 20°. Steady-state stagnation heating ranged from 239 kW/m^2 (21.1 Btu/ft^2-sec) to 395 kW/m^2 (34.8 Btu/ft^2-sec) with heat pipes operating at temperatures of 883 K (1130° F) and 922 K (1200° F), respectively.

A simple analytical technique was used to determine startup, transient, and steady-state performance of the heat pipes during testing. Experimental results agreed well with calculated results for the thermal behavior of the leading edge. Results verified successful operation of the leading edge for all tests, including the design condition which simulated the reentry heating environment of a Phase B shuttle orbiter.

17. Key Words (Suggested by Author(s)) Heat pipes Temperature control Leading-edge cooling Space shuttle orbiters Heat transfer	18. Distribution Statement Unclassified - Unlimited Subject Category 77	
19. Security Classif. (of this report) Unclassified	20. Security Classif. (of this page) Unclassified	21. No. of Pages 41	22. Price* $4.00

ANALYSIS AND RADIANT HEATING TESTS OF A HEAT-PIPE-COOLED LEADING EDGE

Charles J. Camarda
Langley Research Center

SUMMARY

The performance of a heat-pipe-cooled leading edge was investigated experimentally and analytically. The test model and radiant heaters were positioned to simulate aerodynamic heating distributions and gravity effects at angles of attack of $0°$, $10°$, and $20°$. Steady-state stagnation heating ranged from 239 kW/m^2 (21.1 Btu/ft^2-sec) to 395 kW/m^2 (34.8 Btu/ft^2-sec) with heat pipes operating at temperatures of 883 K ($1130°$ F) and 922 K ($1200°$ F), respectively.

A simple analytical technique was used to determine startup, transient, and steady-state performance of the heat pipes during testing. The analysis calculates temperatures by a lumped-system method which uses a volumetric heat capacity per unit length of heat pipe. Rates of continuum vapor region growth were determined by satisfying simple energy balances. Experimental results agreed well with calculated results for the thermal behavior of the leading edge. Results verified successful operation of the leading edge for all tests, including the design condition which simulated the reentry heating environment of a Phase B shuttle orbiter.

INTRODUCTION

The wing leading edge is a critical area of reusable space transportation systems because of the hostile thermal environment experienced during Earth entry. Temperature levels along the stagnation line of an uncooled leading edge can exceed the thermal-structural capabilities of metals and thus necessitate the use of ceramic or ablative materials. In addition, large temperature gradients produced by steep variations in the aerodynamic heating near the stagnation line can induce thermal stresses in uncooled leading edges (ref. 1) unless complex load-alleviating features are incorporated in the structural design.

The use of heat pipes has been examined as a means of lowering the peak temperatures and alleviating the thermal gradients associated with leading edges of reusable reentry vehicles (refs. 1 to 4). Results of references 2 and 3, which compare heat-pipe-cooled with ablative, carbon-carbon, and coated-columbium leading edges, suggest the viability of a heat-pipe-cooled concept. As described in reference 1 and in appendix A on heat-pipe operation, heat pipes can efficiently transport heat from the hot stagnation region to cooler aft surfaces of the wing, where the heat is radiated to free space.

The purpose of this study is to investigate, analytically and experimentally, the performance of a heat-pipe-cooled leading edge exposed to varying heating levels and distributions representative of different angles of attack. The experimental investigation used an approximately 1/2-scale test model which

was designed and fabricated, as described in references 3 and 4, to establish
the feasibility of a full-scale leading-edge concept for a Phase B shuttle orbi-
ter. The model, which consists of 12 sodium-filled Hastelloy X heat pipes, was
designed to reduce temperatures of the leading edge from 1590 K (2400° F) to
less than 1285 K (1850° F) for a cold-wall stagnation heat flux of 408 kW/m^2
(36 Btu/ft^2-sec).

This paper presents experimental results from radiant heating tests of the
leading-edge model in which maximum cold-wall stagnation heating ranged from
239 to 395 kW/m^2 (21.1 to 34.8 Btu/ft^2-sec). The model and heaters were posi-
tioned to simulate aerodynamic heating distributions and gravity effects for
level flight at angles of attack of 0°, 10°, and 20°. In the first six tests
heating levels were increased in steps until the desired test conditions were
reached. The final test simulated the cold-wall reentry heating environment of
a Phase B shuttle orbiter.

In addition, this paper presents calculated results which were obtained by
using a method of analysis similar to those presented in references 1 and 5.
Heat-pipe startup behavior and temperatures were calculated by a lumped-system
technique which satisfied simple energy balances. Comparisons of calculated and
experimental results for two tests are presented.

SYMBOLS

Values are given in both SI Units and U.S. Customary Units. Measurements
and calculations were made in U.S. Customary Units.

A	cross-sectional area, m^2 (ft^2)
a	speed of sound, m/s (ft/sec)
C	volumetric heat capacity per unit length of heat pipe, J/m-K (Btu/ft-°F)
c_p	specific heat at constant pressure, J/kg-K (Btu/lbm-°F)
D	diameter of vapor space, m (ft)
F_{12}	geometric form factor from heater to leading edge
g_c	dimensional constant, g-m/N-s^2 (lbm-ft/lbf-sec^2)
h_{fg}	latent heat of varporization, J/kg (Btu/lbm)
k	ratio of specific heats of vapor
L	length, m (ft)
M	molecular weight, g/mole (lbm/mole)
$\dot{Q}$	heat input, W (Btu/sec)

2

$\dot{Q}_a$ axial heat transport, W (Btu/sec)

$\dot{Q}_r$ heat lost by radiation, W (Btu/sec)

$\dot{Q}_s$ sonic heat transport rate, W (Btu/sec)

q   heat flux, W/m^2 (Btu/ft^2-sec)

$\bar{q}$ heat per unit length, W/m (Btu/ft-sec)

R   universal gas constant, J/mole-K (ft-lbf/mole-^oF)

s   chordwise surface distance measured from nose, m (ft)

s_T total surface distance from nose to end of leading edge, m (ft)

T   temperature, K (^oF)

T^* temperature above which continuum flow conditions are assumed to exist in the vapor space, K (^oF)

t   time, s (sec)

Δt incremental time step, s (sec)

x   variable length along axis of heat pipe, m (ft)

y   coordinate measured from center of model along span (shown in table I), m (ft)

α angle of attack, deg

ϵ porosity

θ angle measured from the horizontal, deg

λ mean free path, m (ft)

μ viscosity, g/m-s (lbm/ft-sec)

ρ density, g/m^3 (lbm/ft^3)

Subscripts:

c   condenser

e   evaporator

hx   Hastelloy X

ℓ lower

m	molecular flow
max	maximum
Ni	nickel
Na	sodium
t	stagnation conditions
ss	stainless steel
u	upper
v	vapor

MODEL AND APPARATUS

A heat-pipe-cooled leading edge was designed for a Phase B shuttle orbiter, and an approximately 1/2-scale thermal model was designed and fabricated (refs. 3 and 4) to verify feasibility of the concept. Sodium was chosen as the working fluid because of its high heat transport capacity and its compatibility with nickel-base superalloys at expected operating temperatures. The leading edge was coated with a high-emissivity ceramic paint to facilitate heat rejection by radiation from its surface.

The test model, shown in figure 1, is 15 cm (6 in.) in span and has a chord length of 56 cm (22 in.). It consists of 12 sodium-filled heat pipes brazed to the inner surface of a thin (0.051-cm (0.02-in.)) Hastelloy X skin. The heat pipes are Hastelloy X tubes with an outer diameter of 1.27 cm (0.5 in.), a wall thickness of 0.127 cm (0.05 in.), and a wick thickness of 0.089 cm (0.035 in.). The wick consists of seven alternate layers of 100- and 200-mesh stainless steel screen and is a concentric annulus design. (See fig. 1.) The 200-mesh screen is located at the outer and inner surfaces of the wick to insure good liquid contact with the tube wall and a high capillary pumping capability. Both the sides and the back of the test model are covered with insulation to prevent heat loss from the inner cavity of the model during testing.

The test model and test conditions differed from the full-scale design and flight conditions in three areas: (1) the test model thickness was about one-half the orbiter wing thickness, (2) testing took place in a 1g envionment, and (3) test angles of attack ranged from 0° to 20°. The cross-sectional area of the test-model wick was scaled, as described in reference 3, to equilibrate the capillary pumping head for both the flight test and a 10° angle-of-attack test. Satisfactory performance of the test model when pitched 10° upward from the horizontal for typical reentry heat loads would, therefore, insure adequate wick capability of the flight design. An explanation of heat pipe operation and its application to leading-edge cooling is given in appendix A.

Three radiant heaters, shown in figure 2, were used to simulate aerodynamic heating distributions over the surface of the model. Each heater was 30.5 by

4

30.5 cm (1 by 1 ft) and consisted of 16 quartz iodine lamps. Each lamp had an output of 6 kW (5.69 Btu/sec) at a rated voltage of 480 V and an overall lighted length of 24.76 cm (9.75 in.). The lamps in each heater were spaced 1.27 cm (0.5 in.) apart in front of a gold-plated water-cooled reflector. The method used to determine the position and orientation of the heaters is described in appendix B.

INSTRUMENTATION AND DATA ACQUISITION

Twenty-seven chromel-alumel thermocouples, located as shown in table I, were spot-welded to the outer surface of the heat pipes inside the model. Two thermocouples (thermocouples 1 and 2) were bonded to the backside of the skin between two heat pipes near the stagnation region, where maximum temperatures were predicted.

Twenty-three heat-flux gages (18 thermopile gages and 5 water-cooled calorimeter gages), located as shown in table II, were used to measure the incident heat flux distribution over the surface of the model. As shown in figure 2, the thermopile gages were bonded to the surface of the model and the calorimeter gages were attached to the side of the model. The thermopile gages were calibrated to measure cold-wall heating rates as a function of gage surface temperature and gage output. Because of the nonlinearity of the gage response, a polynomial regression analysis was used to obtain a relation between gage output, incident heat load, and gage surface temperature. Three calorimeter gages (gages 1 to 3) were used in separate feedback control loops to regulate output of each lamp bank individually according to preprogrammed heating histories.

The outputs of the thermocouples and thermopile gages were recorded by a steady-state recording system sampling at a rate of 20 frames per second.

TESTS

The leading-edge model was tested at simulated angles of attack of 0°, 10°, and 20° at maximum cold-wall stagnation heating levels of 239 to 395 kW/m^2 (21.1 to 34.8 Btu/ft^2-sec). (See table III.) Angle of attack was simulated by orienting the model at an angle with respect to the horizontal to obtain the desired gravity effect and by positioning the radiant heaters to provide a heating distribution representative of the aerodynamic heating distribution at that angle. (See appendix B.) The normalized heating distribution was kept constant while the magnitude of heating varied following a preprogrammed 30-min heating history. In the first six tests, the magnitude of heating was increase slowly in step increments to avoid the potential startup problems described in appendix A. For test 1 (the only one of the first six tests discussed in detail), the stagnation heat input was increased over a period of 16 min to a maximum value of 239 kW/m^2 (21.1 Btu/ft^2-sec). The heating distribution was symmetric, as shown in figure 3, and the model angle of attack was zero.

In the final test (test 7) the heat pipe leading edge was subjected to a thermal history which simulated the design transient reentry heating described in reference 3. The model was pitched 10° up from the horizontal during testing

and a simulated aerodynamic heat load representative of that for 10° angle of attack, shown in figure 4, was maintained over the model surface.

RESULTS AND DISCUSSION

Table III lists the maximum cold-wall stagnation heat flux and maximum heat pipe operating temperature of each test. The inconsistent variation of maximum temperature and heat flux between tests 1 and 2 is believed to be the result of the unexplained drop in heat flux at the stagnation point (see fig. 3) during test 1. The heat pipe was successfully operated at each of the tabulated conditions with no hot spots or other abnormalities that would be indicative of an approach to one of the operating limits. (See appendix A.) The capillary pumping limit (appendix A) was not approached during the tests for any of the angles of attack tested (0°, 10°, and 20°); variations in angle of attack had a negligible effect on heat pipe performance. From the multiple successful tests, it can be inferred that redistribution of liquid sodium during cooldown did not have a deleterious effect on the startup or operation of the heat pipes; a sufficient amount of sodium for startup solidified in the stagnation region and insured continued successful tests.

Because the results of the step heating tests were similar, only the results of tests 1 and 7 are described in detail.

Stepped Heat Input (Test 1)

Based on the results of reference 5, it was anticipated that the heat pipes would exhibit a frontal startup. This type of startup can be expected when heat is applied to a heat pipe in which the working fluid is initially frozen. It occurs because the vapor pressure associated with the solid state is so low that molecular flow conditions, instead of continuum flow conditions required for heat pipe operation, exist in the vapor space. As heat is added, the vapor pressure in the area of highest heat flux increases sufficiently for continuum flow to be established and the heat pipe becomes operational locally. As more heat is added, the continuum region grows into the molecular flow region. This growth is perceived as an abrupt increase in the local temperature as the continuum front passes and the heat pipe becomes operational in that area.

The abrupt increases in the experimental temperature histories at approximately 600 s and 1150 s for $s/s_T = 0.23$ and 0.88, respectively, shown in figure 5, are typical of a frontal startup. Other discontinuities in the slopes of the temperature histories result from the step increases in the heating rates. (See top of figure.) After each increase in heating the temperature increases and reaches a quasi-steady-state value for that level of heating.

The calculated results shown in figure 5, which were obtained by the lumped-system method given in appendix C, provide a surprisingly good approximation of the overall performance of the heat pipe, considering the simplistic representation of the physical model. The good agreement between the calculated and experimental results tends to confirm the sonic limit as the controlling factor in determining the rate of growth of the continuum region, as postulated in the

analysis, and corroborates the results of references 1 and 5. During the startup phase, calculated results underpredict the temperature of the continuum region and overpredict time of passage of the continuum front. One possible explanation for the lower calculated temperature during this phase is that gasdynamic choking of the vapor during startup causes large axial pressure - and hence temperature - gradients, as described in reference 6. Since the mathematical model assumes incompressible vapor flow and an isothermal continuum region, differences in calculated and experimental results occur during this phase of operation.

Calculated values for the steady-state temperatures, at $t \geq 1700$ s, are higher than experimental values by 17 K (30° F). This is probably the result of free convection from the model and heat losses through the insulation covering the back and sides, which were not considered in the analysis. For the levels of heating involved, an approximation of the heat losses by convection from the upper and lower surfaces of the model shows that a 17 to 56 K (30° to 100° F) decrease in operating temperature is possible.

The analysis yields no information on the actual temperature rise rates encountered during the passage of the continuum front. As shown in figure 5, the actual rise rate is considerably less than the instantaneous transition assumed in the analysis, probably because of axial conduction, which was neglected in the analysis.

A more comprehensive summary of the predicted and measured growth of the continuum region is given in figure 6, which is a plot of the continuum region length as a function of time. The approximate time that startup begins, as obtained from the figure, is between 400 and 550 s and occurs at a temperature (fig. 5) between 561 and 728 K (550° and 850° F). The calculated value of temperature above which continuum flow was assumed to occur T^* was 700 K (800° F) (appendix C). The discontinuity in slope of the calculated curve shown in figure 6 is due to the discrete nature of the mathematical model used to determine continuum region growth rates in various sections of the model. Because the model was heated slowly, it takes approximately 750 s, measured from the time continuum flow is initiated at the stagnation region, for the continuum vapor front to reach the ends of the heat pipe. Calculated values, although slightly overpredicting the time of continuum front passage, agree well with experimental values.

Typical axial temperature distributions encountered during the startup and steady-state conditions are shown in figure 7. At times less than 550 s the temperature distribution over the leading edge is similar to that of an uncooled structure, since no continuum flow has been established in the heat pipe. After continuum flow is established, the isothermal continuum region grows, as shown by the curves faired through the experimental data points. At $t = 1500$ s, a relatively isothermal condition exists for an operating temperature of 883 K (1130° F); the maximum temperature difference from the stagnation point to the end of the heat pipe in the upper section of the leading edge ΔT is 67 K (120° F). The maximum steady-state value of ΔT diminishes with increasing operating temperatures; in test 6 this temperature differential reduces to 5.6 K (10° F) for an operating temperature of 1022 K (1380° F).

Comparison of Cooled and Uncooled Leading Edge

As shown in figure 7, temperature gradients for the fully operational heat pipe are small and probably produce negligible thermal stresses. However, during the startup phase, large axial temperature gradients develop and are comparable with those of an uncooled leading edge. At t = 1000 s, for example, an axial temperature gradient of 4370 K/m (2400° F/ft) occurs at station s/s_T = -0.75. From figure 8, the maximum calculated thermal gradient of an uncooled leading edge at steady-state conditions occurs at s/s_T = ±0.1 and is 6560 K/m (3600° F/ft). The benefits obtained by using heat pipes to cool the leading edge of a high-speed vehicle can be seen in figure 8 by comparing the radiation equilibrium temperature distribution of an uncooled leading edge with the temperature distribution of the heat-pipe-cooled leading edge for the same heating environment. Once fully operational, the heat-pipe-cooled leading edge virtually eliminates axial temperature gradients and reduces peak temperatures by 583 K (1050° F). Available superalloys can thus be used in the construction of the leading edge.

Shuttle Reentry Simulation Tests

Figure 9 shows the temperature history of three locations along the upper surface of the leading edge. The heat pipe was fully operational before a peak reentry heat flux of 390 kW/m^2 (34.4 Btu/ft^2-sec) was reached. The simple analysis method proved accurate in predicting heat pipe startup behavior for shuttle reentry conditions. As in the stepped heat input tests, differences between calculated and experimental values of temperature probably occur because of large axial vapor temperature gradients during startup and convective heat losses at high operating temperatures.

Because of the unsymmetric heating distribution at a 10° angle of attack (fig. 4), the calculated rates of continuum region growth in the upper and lower sections of the leading edge, shown in figure 10, are no longer symmetric. The higher heat load over the lower surface caused the continuum region to propagate faster there and reach the end of the tube in the lower section 100 s before it did in the upper section. Because of the high rate of heat addition, the heat pipes became fully operational only 350 s after continuum flow was established in the evaporator.

This test verified that a sodium heat-pipe-cooled leading edge could withstand reentry heating conditions of a Phase B shuttle orbiter and could reduce peak temperatures sufficiently to allow the use of existing superalloys in its construction. The test also established that the time required for the heat pipes to become fully operational is adequate for the design condition. No serious limiting conditions were encountered during testing, and once the heat pipes were fully operational, they remained nearly isothermal with a maximum temperature difference from evaporator to condenser of 5.6 K (10° F) at an operating temperature of 939 K (1230° F).

CONCLUDING REMARKS

The thermal behavior of a heat-pipe-cooled leading-edge test model subjected to anticipated Earth-entry thermal loads has been investigated. The test model and radiant heaters were used to simulate aerodynamic heating and gravity effects for level flight at angles of attack of 0°, 10°, and 20° with variations in maximum stagnation heating from 239 to 395 kW/m^2 (21.1 to 34.8 Btu/ft^2-sec). Seven tests were conducted, one of which simulated the transient reentry heating environment of a Phase B shuttle orbiter.

No serious startup or other limiting conditions developed during testing; variations in angle of attack had a negligible effect on heat-pipe operation. Also, redistribution of the liquid sodium during cooldown did not have a deleterious effect on restartup of the heat pipes for successive tests. The heat pipes remained nearly isothermal during steady state, the temperature difference between the evaporator and condenser being a maximum of 67 K (120° F) at a maximum operating temperature of 883 K (1130° F) and a minimum of 5.6 K (10° F) at a maximum operating temperature of 1022 K (1380° F).

Although results of the tests verified that the model could withstand a reentry aerodynamic heating environment, large axial temperature gradients produced during the startup phase could lead to large thermal stresses. Such conditions produced during this phase could become critical design considerations.

An analysis method based on a relatively crude mathematical model which used a lumped-system technique to determine temperatures proved accurate in predicting the thermal behavior of the leading edge. Rates of continuum vapor region growth during the startup transient which were predicted using simple energy balances agreed well with experimental results.

Langley Research Center
National Aeronautics and Space Administration
Hampton, VA 23665
May 23, 1977

APPENDIX A

HEAT PIPE OPERATION

Description

A heat pipe is an efficient heat transfer device which can transport heat energy nearly isothermally at high rates and over long distances without the need for external pumping. Figure 11 is a schematic diagram of heat pipe operation as applied to leading-edge cooling. A heat pipe is composed of a container, a wick, and a working fluid. A high local heat input to one section of the leading edge (evaporator section) is conducted through the skin and container wall into the wick—working-fluid matrix, where it is absorbed by the evaporation of the working fluid. The heated vapor then flows, because of a pressure differential, from the hot evaporator region to the cooler aft surfaces of the leading edge (condenser sections), where it condenses and gives up its stored heat. The heat is then conducted radially through the wick—working-fluid matrix and container wall and is rejected by radiation to free space. The cycle is completed with the return flow of liquid condensate to the evaporator section by the capillary action of the wick. The location and extent of the evaporator and condenser sections, which are by definition areas in which there is a net heat inflow or outflow, respectively, are dependent upon the magnitude and distribution of heating and will vary to satisfy an overall energy balance.

Because of the mechanism of heat transfer involved, evaporation and condensation, heat pipes using working fluids with high latent heats of vaporization can achieve very high heat transfer rates. Heat pipes are therefore suited for applications involving structural cooling and/or isothermalization. As illustrated in figure 11, a heat-pipe-cooled leading edge can accept a high net heat input over a small area, the evaporator section, and reject it over a larger area, the condenser section. This redistribution of heating can cause a considerable reduction in peak stagnation temperatures, often to a level compatible with a metallic structural design.

Heat Transport Limitations

A given heat pipe can operate over a range of temperatures; however, at each temperature there is a maximum axial heat transport capacity above which normal heat pipe operation is disrupted. Four heat pipe operational limits are considered: the sonic limit, the entrainment limit, the capillary pumping or wicking limit, and the boiling limit. The maximum axial heat transport capacity at a particular heat pipe operating temperature is governed by the lowest calculated operating limit at that temperature. The four limits are described in the following sections.

Sonic limit.- Since the primary mode of heat transfer in a heat pipe is by the absorption and rejection of energy by the latent heat of vaporization of the working fluid, the axial heat transfer, and hence mass transfer, must accommodate the net heat input to the evaporator region. A high heat input rate or a low vapor density can cause the vapor velocity to become sonic in order to attain the

necessary axial heat transport required. When the vapor velocity becomes sonic, flow choking limits the amount of axial heat transfer. Although the sonic limit does not normally cause failure, it can increase the operating temperature and lead to other operating limits.

Entrainment limit.- In a heat pipe the liquid and vapor are usually in direct contact and are flowing in opposite directions. The high-velocity vapor exerts a drag force on the liquid, which is resisted by the surface tension of the working fluid. If this drag force is sufficiently high, some of the returning liquid condensate can become entrained or trapped in the vapor passage and thus reduce the amount of liquid in the wick flowing to the evaporator section. This could lead to dryout of the wick in the evaporator section and overheating.

Capillary pumping limit.- The capillary pumping limit is reached when the surface-tension pumping capability of the wick is just sufficient to provide the liquid mass flow rate needed to balance the applied heating rate. If this limit is exceeded, the pressure difference between the liquid and vapor, which is balanced by the surface tension of the curved liquid-vapor interface in the wick pores, will cause the destruction of the interface; liquid will flow into the vapor space and the heat pipe will overheat in the evaporator section. The capillary pumping limit can be increased by reducing the liquid and/or vapor flow resistance in the axial direction and by reducing the wick pore size at the liquid-vapor interface in the evaporator section.

Boiling limit.- Vaporization of the working fluid normally occurs in the evaporator section of the heat pipe at the liquid-vapor interface. At high heat input levels, however, the superheated liquid can reach a critical value at which boiling can occur near the tube wall. The boiling limit is reached when the heating rate is high enough to cause the formation of a continuous vapor film (film boiling) at the tube wall which inhibits radial heat transfer to the liquid. This limit is usually not a severe problem with heat pipes using liquid-metal working fluids because of the high thermal conductivity of the working fluid and the large amount of superheat needed to initiate boiling.

Calculated heat transfer performance limits.- Figure 12 is a design envelope for the leading-edge test model at angles of attack of 0° and 10°. The heat transported axially from the evaporator to the condenser section is plotted against the operating temperature of the heat pipe. References 7 and 8 were used to obtain material property data as a function of temperature. Values for the entrainment and sonic limits were obtained from references 1 and 6, respectively. The wicking limit, or capillary pumping limit, was determined by using equations given in reference 9. As shown in figure 12, the effect of gravity aids the capillary pumping action in the upper section and raises the wicking limit accordingly. The calculation of the boiling limit is highly dependent on the choice of the effective radius of the critical nucleation cavity. Several methods were used to calculate the boiling limit and all methods indicated that the maximum desired test heating rate was below this limit.

The feasible operating region shown in figure 12 is bounded by the sonic limit at low operating temperatures and by the entrainment limit and wicking limit at higher temperatures. The boiling limit was not an active constraint for temperatures less than 1255 K (1800° F) and was therefore not plotted. The

11

calculated heat transfer performance limits were monitored in the analysis (appendix C) to identify possible abnormalities in heat-pipe operation.

Startup

For liquid-metal heat pipes, operation from ambient conditions requires proper startup of the heat pipe from a frozen state (i.e., the working fluid is solid). During ambient conditions the vapor density is extremely low and molecular flow conditions prevail throughout the heat pipe; heat input increases the vapor density in the heated region and a continuum flow condition is eventually reached. The continuum region grows until it reaches the ends of the heat pipe, or stops short of the ends of the heat pipe because of a lower-than-design heating condition. This high-temperature continuum region melts the solid sodium in adjacent sections of the heat pipe as it propagates down the vapor passage. If the heat is input at a high rate, dryout of the liquid sodium in the evaporator section can occur before sufficient sodium is melted to replenish it. Also, large pressure, and hence temperature, gradients occur during the startup phase and must be accounted for in the design. The startup phase begins at the onset of continuum flow in the evaporator and ends when continuum region growth either ceases or encompasses the entire vapor space of the heat pipe.

Further detailed explanations of heat pipe theory and limit calculations can be found in references 1 and 5 to 14.

APPENDIX B

CONFIGURATION OF RADIANT HEATERS

The position and orientation of the radiant heaters were determined by an analysis of the geometric form factors between the heaters and the heat pipe leading edge. It was possible to use these form factors, which were generated using CONFAC II (ref. 15), to assess the performance of the heaters, since for a uniform heating source the normalized form-factor distribution is indicative of the normalized incident-heating distribution over the model.

A configuration consisting of a single vertical heater was analyzed, and the results indicated the need for auxiliary heaters to simulate the cold-wall reentry heating distributions of reference 3 over the aft surfaces of the model for angles of attack of 0°, 10°, and 20°.

The leading edge was modeled by twenty-three 5.08- by 0.64-cm (2- by 0.25-in.) rectangular elements, which represented a slice from the center portion of the leading edge. Each lamp bank was modeled by six 5.08- by 30.5-cm (2- by 12-in.) rectangular elements. The form factors of each element were then summed and normalized for each configuration analyzed.

Results of the form-factor analysis of a heating simulation for 0° angle of attack and a single vertical radiant heater are shown in figure 13. The leading edge was positioned in the center of the heater at a horizontal distance of 2.54 cm (1 in.) from the heater. This distance was large enough to insure uniform heating from the lamp bank. For the single heater configuration the simulation of the normalized aerodynamic heating over the aft section of the leading edge was poor, with a maximum difference of 10 percent occurring at $s/s_T = \pm 0.33$.

The addition of auxiliary heaters was investigated in an attempt to improve the distribution over the aft section of the leading edge and to provide for heating distributions at other angles of attack. Normalized form-factor distributions for a single auxiliary heater at three different orientations ($\theta = 10°$, 20°, and 30°) are shown in figure 14. These distributions were scaled and added to the form factors for the single heater so that the sum of the form factors of a three-heater configuration would duplicate the theoretical aerodynamic heating distribution of reference 3 at $s/s_T = 0.33$. During the tests calorimeters at $s/s_T = 0.0$ and ± 0.33 were used to control the output of the vertical heater and upper and lower auxiliary heaters so that the heating level at these locations would match the theoretical cold-wall heating.

Based on the form-factor analyses the heater configurations presented in figure 15 were selected as providing the best heating distributions for the three angles of attack (0°, 10°, and 20°). The desired (ref. 3), calculated, and measured heating distributions for angles of attack of 0° and 10° are shown in figures 3 and 4, respectively. The poorer agreement for the thermopile gages in figure 4 is believed to result from a loss of accuracy of the gages because of gage bonding problems, which increased during testing.

APPENDIX C

ANALYSIS

Description

The analysis method used to model the startup, transient, and steady-state performance of a heat-pipe-cooled leading edge is similar to but somewhat more general than that of reference 1. Although most of the assumptions involved are identical, the present method uses more discrete sections to model the leading edge and an expression for the sonic heat transport rate $\dot{Q}_S$ which incorporates axial compressibility effects in its computation. Also, an a priori knowledge of the lengths and locations of evaporator and condenser sections is not necessary. As in reference 1, a lumped-system method is used to analyze a single heat pipe which is representative of the complete leading edge.

In the analysis it is assumed that the temperature of the heat pipe is initially below the melting point of the working fluid (i.e., frozen) and, consequently, the vapor pressure is low. Thus, molecular flow conditions exist throughout the heat pipe, and axial heat transfer is very low. As heat is applied, the temperature and vapor pressure of the most highly heated region increase until continuum flow conditions are established in that region. Within the continuum flow region the effective axial coefficient of heat transfer is very large; thus a nearly uniform temperature is maintained throughout the region. Additional heating causes the temperature of the continuum region to increase and the continuum front to grow into the molecular flow region. The growth rate of the continuum region is dependent upon the temperature of the molecular region and the rate of axial heat transfer out of the continuum region.

Major Assumptions

The assumptions made in the present analysis are as follows:

(1) All heat is absorbed or rejected through the external skin surface; that is, all heat pipe surfaces except the external skin are perfectly insulated. All heat is input by radiation from the quartz lamp heaters and is rejected by radiation to ambient temperature.

(2) At any axial station the temperature of the heat pipe is uniform.

(3) The heat capacity of the heat pipe can be represented by an effective heat capacity per unit heat pipe length which is dependent upon temperature. The heat of fusion of the working fluid is neglected.

(4) Molecular flow occurs when the mean free path of sodium molecules is greater than 1 percent of the vapor-space diameter; continuum flow exists when the mean free path is less than or equal to 1 percent of the vapor-space diameter.

14

(5) Axial heat transfer and heat rejection by radiation are negligible in the molecular flow region.

(6) The temperature is uniform throughout the continuum flow region.

(7) An evaporator (condenser) is a section, within the continuum flow region, in which the net external heat flow is into (out of) the heat pipe; stored heat is not accounted for.

(8) During startup, sonic conditions exist at the evaporator exit or exits and the axial heat transported to the condenser sections is $\dot{Q}_s$.

Initiation of Continuum Flow

Continuum flow is initiated in the region of highest heat input. It is assumed to occur, as in reference 1, when the mean free path λ is equal to or less than 0.01D. The calculated value of temperature at which continuum flow is considered to exist in the vapor space T^* is determined from kinetic gas theory by use of the following equation (from ref. 16, p. 274, in the present notation):

$$T^* = \frac{\pi M}{2 g_c R}\left(\frac{\mu_v}{\rho_v \lambda}\right)^2 \tag{C1}$$

Since μ_v and ρ_v are temperature dependent, several iterations of equation (C1) were required to produce a value of T^* which satisfied the equality. A value for T^* of 700 K (800° F) was obtained for the model with D = 0.84 cm (0.33 in.).

Sonic Flow Limit

When continuum flow is established, axial heat transfer from the evaporator section becomes substantial. During startup, axial heat transport is assumed to occur at the exit or exits of the evaporator section at a rate $\dot{Q}_s$, the sonic heat transport rate. The equation used to calculate $\dot{Q}_s$ (from ref. 6, in the present notation) is as follows:

$$Q_s = \frac{\rho_v a h_{fg}(\pi/4)D^2}{\left[2(k+1)\right]^{1/2}} \tag{C2}$$

where a is the speed of sound, D is the diameter of the vapor space, ρ_v is the vapor density, and k is the ratio of specific heats of the vapor. This equation assumes one-dimensional compressible fluid flow and determines $\dot{Q}_s$ at the evaporator exit from conditions at the beginning of the evaporator. Although this is seemingly inconsistent with the assumption of uniform continuum region temperature, it tends to increase the accuracy of calculated continuum region temperature during the startup period.

APPENDIX C

Effective Volumetric Heat Capacity

An effective volumetric heat capacity per unit length of heat pipe was calculated as a function of temperature by the following equation:

$$C = (\rho c_p)_{hx} A_1 + (\rho c_p)_{Ni} A_2 + (\rho c_p)_{hx} A_3 + \epsilon(\rho c_p)_{Na} A_4 + (1 - \epsilon)(\rho c_p)_{ss} A_4 \qquad (C3)$$

where A_1, A_2, A_3, and A_4 are the cross-sectional areas of the Hastelloy X skin, nickel braze alloy, Hastelloy X tube, and stainless steel wick, respectively. The effective heat capacity was used to calculate the temperature of the molecular and continuum flow regions of the heat pipe.

Calculation of Molecular Flow Region Temperatures

The expression for the temperature of the molecular flow region is obtained by equating the external heat input to the amount of heat stored in that region. The temperature of the molecular flow region T_m is determined by the following equation:

$$T_m(t+\Delta t) = T_m(t) + \frac{\bar{q}\,\Delta t}{C_m} \qquad (C4)$$

where $\bar{q}$ is the external heat input per unit length of the molecular flow region, Δt is the incremental time step, $T_m(t)$ is the temperature of the molecular flow region at time t, $T_m(t+\Delta t)$ is the temperature of that region at time $t + \Delta t$, and C_m is the effective volumetric heat capacity of the molecular flow region per unit length of heat pipe at temperature $T_m(t)$.

Calculation of Continuum Flow Region Temperatures

Figure 16(a) is a diagram of a heat pipe which has not become fully operational. The continuum flow region consists of an evaporator section and two condenser sections (upper and lower). The lengths and locations of the continuum, condenser, and evaporator sections, shown in the figure, are used in the following equations to determine the temperature of the continuum region.

If the continuum region has not reached either end of the heat pipe, the temperature is, from energy balance considerations,

$$T(t+\Delta t) = T(t) + \frac{\left[(\dot{Q} - \dot{Q}_r)_e - 2\dot{Q}_s\right]\Delta t}{Cx_e} \qquad (C5)$$

where $\dot{Q} - \dot{Q}_r$ is the net heat input to a region, x_e is the length of the evaporator section, and $\dot{Q}_s$ is the sonic heat transport limit at temperature $T(t)$.

If the continuum region reaches the end of the heat pipe in the upper region only, the equation is

$$T(t+\Delta t) = T(t) + \frac{\left[(\dot{Q} - \dot{Q}_r)_e + (\dot{Q} - \dot{Q}_r)_{c,u} - \dot{Q}_s\right]\Delta t}{C(x_e + x_{c,u})} \tag{C6}$$

Similarly, if the continuum region reaches the end of the heat pipe in the lower region only, the subscript u is changed to ℓ.

If the continuum region reaches both ends of the heat pipe (i.e., the heat pipe is fully operational), the equation is

$$T(t+\Delta t) = T(t) + \frac{\left[(\dot{Q} - \dot{Q}_r)_e + (\dot{Q} - \dot{Q}_r)_{c,u} + (\dot{Q} - \dot{Q}_r)_{c,\ell}\right]\Delta t}{C(L_u + L_\ell)} \tag{C7}$$

Continuum Region Propagation

The equations used to determine continuum region growth in the upper and lower sections of the leading edge are dependent on whether the continuum region propagating into the molecular flow region is an evaporator section or a condenser section. The reason for the dependency is that during startup it was assumed that the heat transport axially was $\dot{Q}_s$ and that this sonic condition occurred at the evaporator exit. Diagrams of both situations, evaporator or condenser propagating into a molecular flow region, are shown in figures 16(b) and 16(c). The equation used to calculate continuum region growth is

$$x(t+\Delta t) = x(t) + \frac{\dot{Q}_a \Delta t}{C\,T(t+\Delta t) - C_m\,T_m(t)} \tag{C8}$$

where for an evaporator propagating into a molecular flow region,

$$\dot{Q}_a = \dot{Q}_s$$

and for a condenser propagating into a molecular flow region,

$$\dot{Q}_a = (\dot{Q} - \dot{Q}_r)_c + \dot{Q}_s - \frac{Cx_c\left[T(t+\Delta t) - T(t)\right]}{\Delta t}$$

where $\dot{Q}_a$ is the heat transported axially from the continuum region into the incremental volume; $x(t)$ and $x(t+\Delta t)$ are the lengths of the continuum region at times t and $t + \Delta t$, respectively; and C_m is the effective volumetric heat capacity of the molecular flow region.

Mathematical Model

A single heat pipe, shown in figure 17, was analyzed to determine the performance of the leading edge during testing. The heat pipe is divided into six sections over which heat input is uniform. Sections 1u and 1ℓ were assumed to be initial evaporator sections. To reduce modeling errors, the lengths of these sections were chosen to be small ($L_{1u} = L_{1\ell} = 5.08$ cm (2 in.)) because of

the steep gradient in heating near the stagnation region. The lengths of the other four sections were $L_{2u} = L_{2\ell} = 10.16$ cm (4 in.) and $L_{3u} = L_{3\ell} = 43.2$ cm (17 in.).

Equations (C2) to (C7) were programmed to calculate continuum and molecular flow region temperatures and continuum vapor front movement in the upper and lower sections of the leading edge during startup. Program termination occurs when either of several criteria are met: a specified time limit or maximum operating temperature is reached or a steady-state convergence criterion is satisfied. A logic flow diagram of the program is shown in figure 18.

REFERENCES

1. Silverstein, Calvin C.: A Feasibility Study of Heat-Pipe-Cooled Leading Edges for Hypersonic Cruise Aircraft. NASA CR-1857, 1971.

2. Niblock, G. A.; Reeder, J. C.; and Huneidi, F.: Four Space Shuttle Wing Leading Edge Concepts. J. Spacecr. & Rockets, vol. 11, no. 5, May 1974, pp. 314-320.

3. Study of Structural Active Cooling and Heat Sink Systems for Space Shuttle. Rep. No. MDC E0638 (Contract No. NAS 8-27708, McDonnell Douglas Astronautics Co. - East), June 30, 1972. (Available as NASA CR-123912.)

4. Design, Fabrication, Testing, and Delivery of Shuttle Heat Pipe Leading Edge Test Modules. Volume II - Final Report. Rep. MDC E0775, McDonnell Douglas Astronautics Co., Apr. 1973. (Available as NASA CR-138673.)

5. Cotter, T. P.: Heat Pipe Startup Dynamics. Heat Pipes, Volume XVI of AIAA Selected Reprint Series, Chang-Lin Tien, ed., Sept. 1973, pp. 42-45.

6. Levy, E. K.: Theoretical Investigation of Heat Pipes Operating at Low Vapor Pressures. Trans. ASME, Ser. B: J. Eng. Ind., vol. 90, no. 4, Nov. 1968, pp. 547-552.

7. Schins, H. E. J.: Liquid Metals for Heat Pipes, Properties, Plots and Data Sheets. EUR-3653 e, European At. Energy Community, 1967.

8. Touloukian, Y. S., ed.: Thermophysical Properties of High Temperature Solid Materials. Macmillan Co., c.1967.
   Volume 2: Nonferrous Alloys.
   Volume 3: Ferrous Alloys.

9. Dunn, P.; and Reay, D. A.: Heat Pipes. Pergamon Press, c.1976.

10. Cotter, T. P.: Theory of Heat Pipes. Heat Pipes, Volume XVI of AIAA Selected Reprint Series, Chang-Lin Tien, ed., Sept. 1973, pp. 11-41.

11. Marcus, B. D.: On the Operation of Heat Pipes. TRW-9895-6001-TU-006, Space Technol. Lab., Inc., May 1965.

12. Levy, E. K.: Effects of Friction on the Sonic Velocity Limit in Sodium Heat Pipes. AIAA Paper No. 71-407, Apr. 1971.

13. Kemme, Joseph E.: Heat Pipe Design Considerations. Heat Pipes, Volume XVI of AIAA Selected Reprint Series, Chang-Lin Tien, ed., Sept. 1973, pp. 52-57.

14. Katzoff, S.: Heat Pipes and Vapor Chambers for Thermal Control of Spacecraft. Thermophysics of Spacecraft and Planetary Bodies - Radiation Properties of Solids and the Electromagnetic Radiation Environment in Space, Gerhard B. Heller, ed., Academic Press, 1967, pp. 761-818.

15. Toups, K. A.: A General Computer Program for the Determination of Radiant-Interchange Configuration and Form Factors - CONFAC II. SID-65-1043-2, North American Aviat., Inc., Oct. 1965. (Available as NASA CR-65257.)

16. Eckert, E. R. G.; and Drake, Robert M., Jr.: Heat and Mass Transfer. Second ed. McGraw-Hill Book Co., Inc., 1959.

TABLE I.- THERMOCOUPLE LOCATIONS
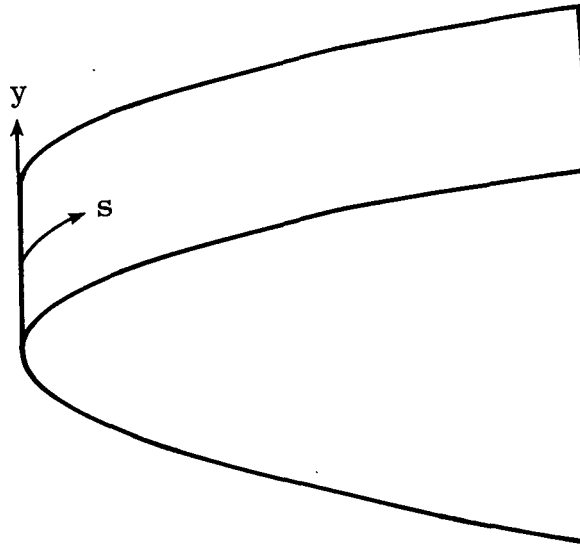
Thermocouple	y		s (a)		Thermocouple	y		s (a)	
	cm	in.	cm	in.		cm	in.	cm	in.
[b]1	0	0	0	0	16	-0.64	-0.25	-10.41	-4.1
[b]2	-1.27	-.5	-3.05	-1.2	17	-.64	-.25	10.41	4.1
3	6.99	2.75			18	-7.62	-3.0	-8.79	-3.46
4	5.72	2.25			19	-.64	-.25	-13.46	-5.30
5	4.45	1.75			20	-.64	-.25	13.46	5.30
6	3.18	1.25			21	7.62	3.0	-26.97	-10.62
7	1.91	.75			22	-.64	-.25	-35.05	-13.8
8	.64	.25			23			-51.23	-20.17
9	-3.18	-1.25			24			51.23	20.17
10	-4.45	-1.75			25			-24.26	-9.55
11	-5.72	-2.25			26			24.26	9.55
12	-6.99	-2.75			27			33.24	13.085
13	-.64	-.25			28			-43.15	-16.99
14	-.64	-.25	6.1	2.4	29			43.15	16.99
15	-.64	-.25	-6.1	-2.4					

[a]Measured from nose along inside surface of heat pipe.
[b]Located between face sheet and two heat pipes.

TABLE II.- HEAT FLUX GAGE LOCATIONS

Gage	y			s (a)	
	cm	in.		cm	in.
Thermopile gages					
1	2.54	1.0		-50.8	-20.0
2	-6.35	-2.5		-30.48	-12.0
3	-6.35	-2.5		-12.7	-5.0
4	2.54	1.0		-2.54	-1.0
5				7.62	3.0
6				-20.32	-8.0
7				12.7	5.0
8				-7.62	-3.0
9				-30.48	-12.0
10				30.48	12.0
11				-12.7	-5.0
12				5.08	2.0
13				0.0	0.0
14	-6.35	-2.5		0.0	0.0
15				2.54	1.0
16				-5.08	-2.0
17				20.32	8.0
18				50.8	20.0
Calorimeter gages					
[b]1	[c]8.89	3.50		[d]0.0	0.0
[b]2				20.32	8.0
[b]3				-20.32	-8.0
4				50.8	20.0
5				-50.8	-20.0

[a]Measured along outer surface from nose.
[b]Gages used to control output of the three lamp banks.
[c]The 2.54-cm (1-in.) diameter calorimeter gages were attached to the side of the leading edge.
[d]Location changed to -1.27 cm (-0.5 in.) for angles of attack of 10° and 20°.

22

TABLE III.- SUMMARY OF TEST CONDITIONS

Test	Angle of attack, deg	Maximum cold-wall stagnation heat flux		T_{max}	
		kW/m^2	Btu/ft^2-sec	K	^{o}F
Stepped heating tests					
1	0	239	21.1	883	1130
2	0	299	26.4	861	1090
3	0	395	34.8	922	1200
4	10	294	25.9	911	1180
5	20	260	22.9	928	1210
6	20	380	33.5	1022	1380
Simulated reentry heating					
7	10	390	·34.4	939	1230
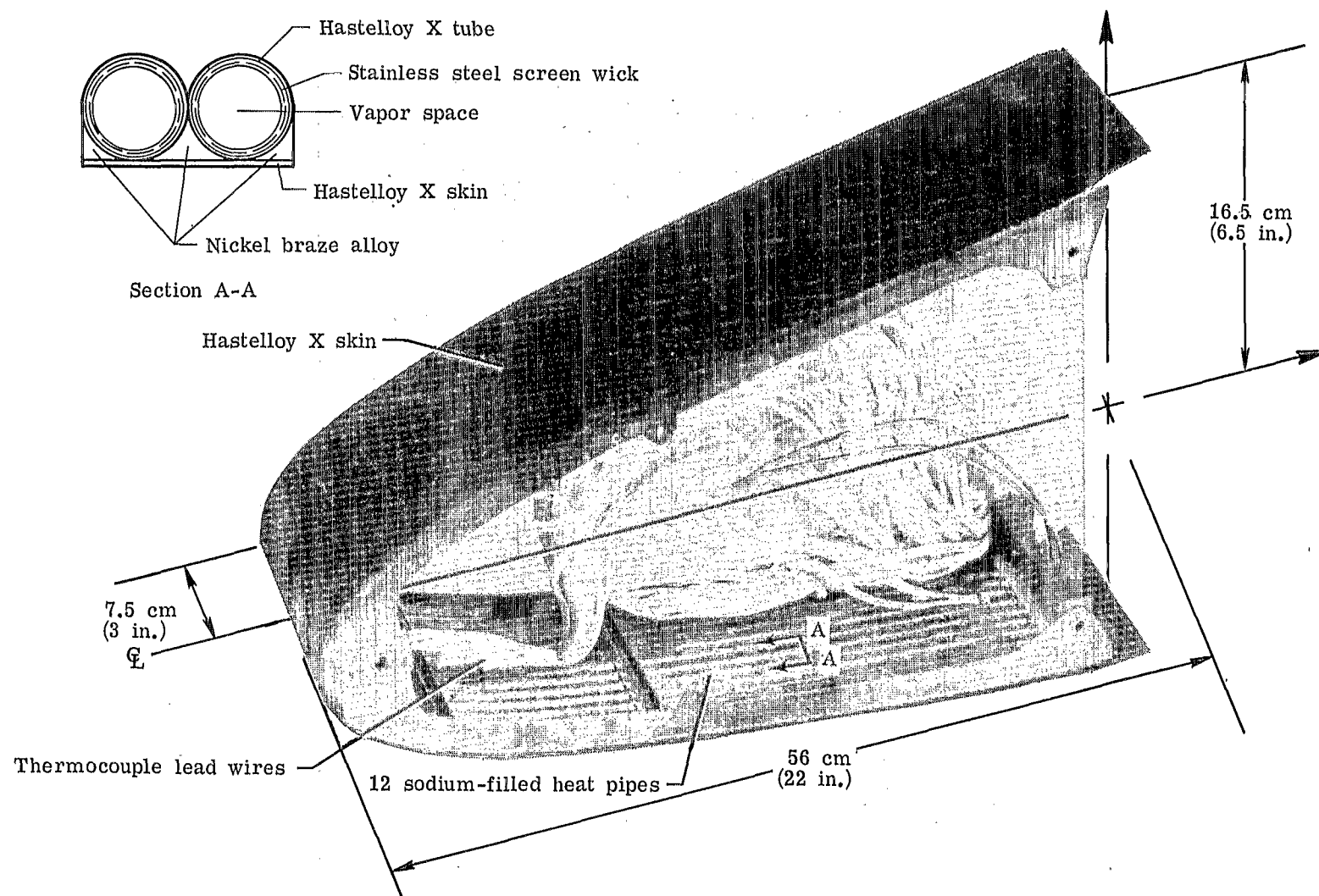
Figure 1.- Heat-pipe-cooled leading-edge test model.

L-74-6010.1

Heaters

Thermopile gages
(typical)

Insulation

Control calorimeter
heat flux gages
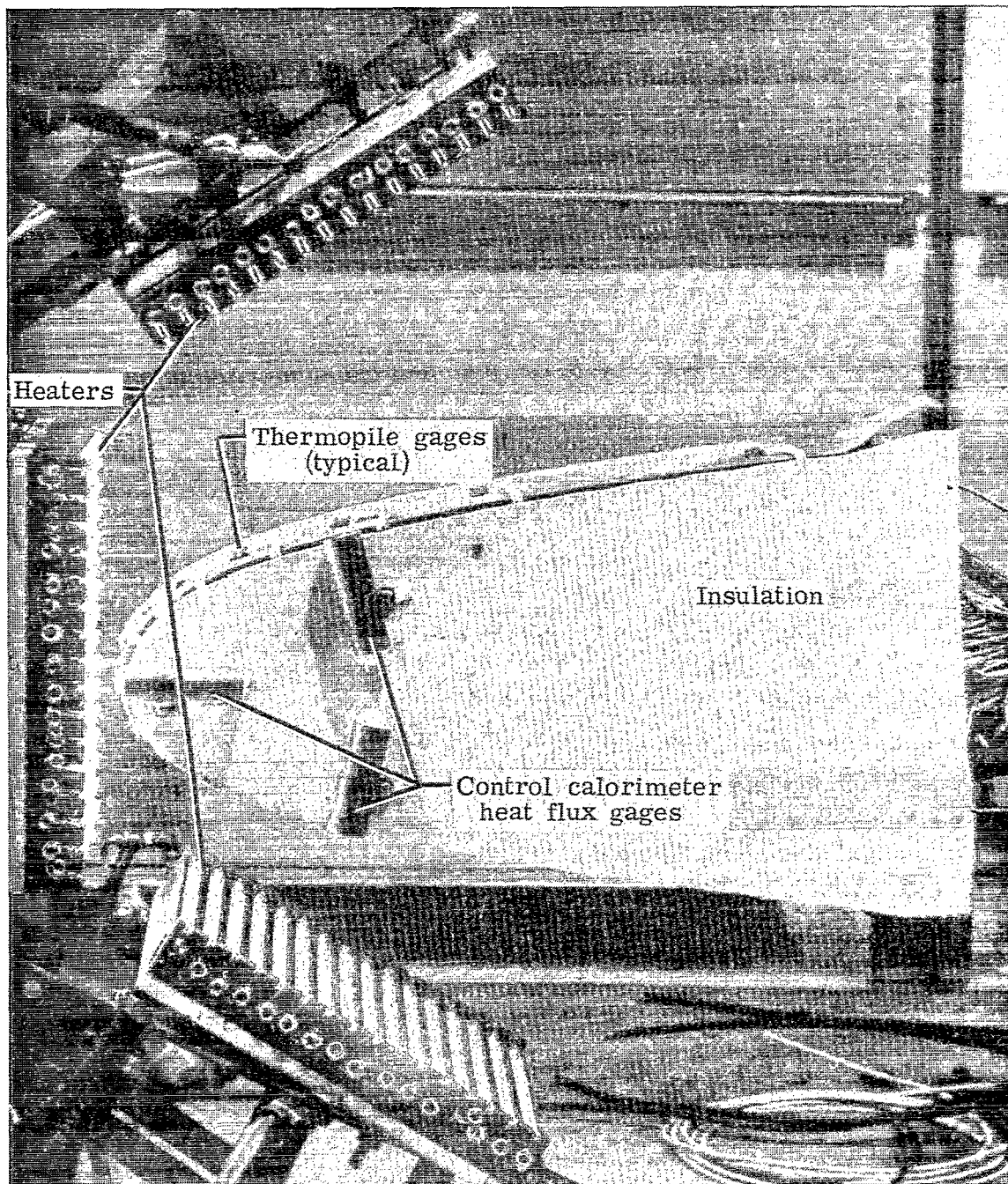
Figure 2.- Heat-pipe-cooled leading-edge model during radiant heating test.
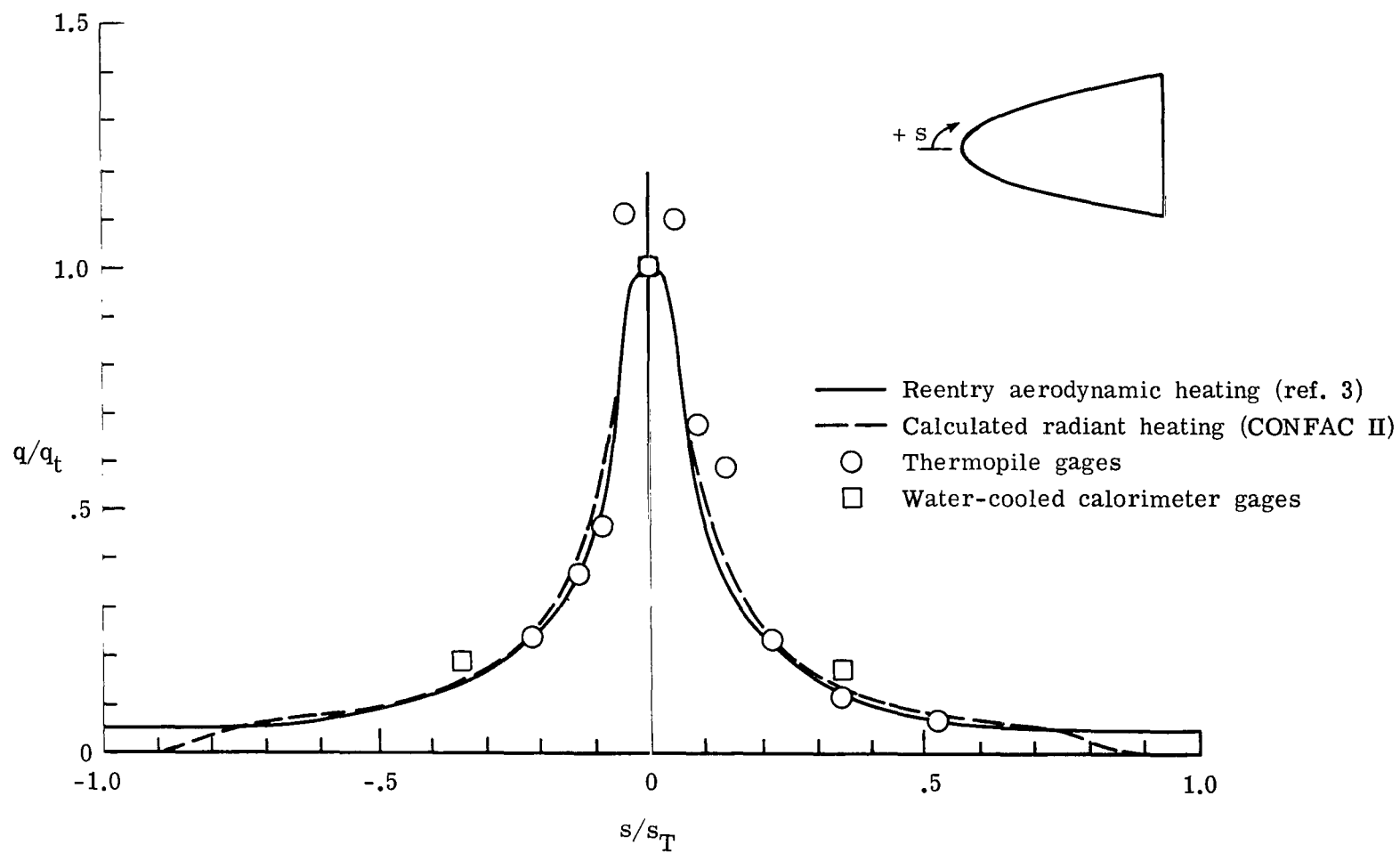
Figure 3.- Normalized cold-wall heating distribution for 0° angle of attack (test 1).
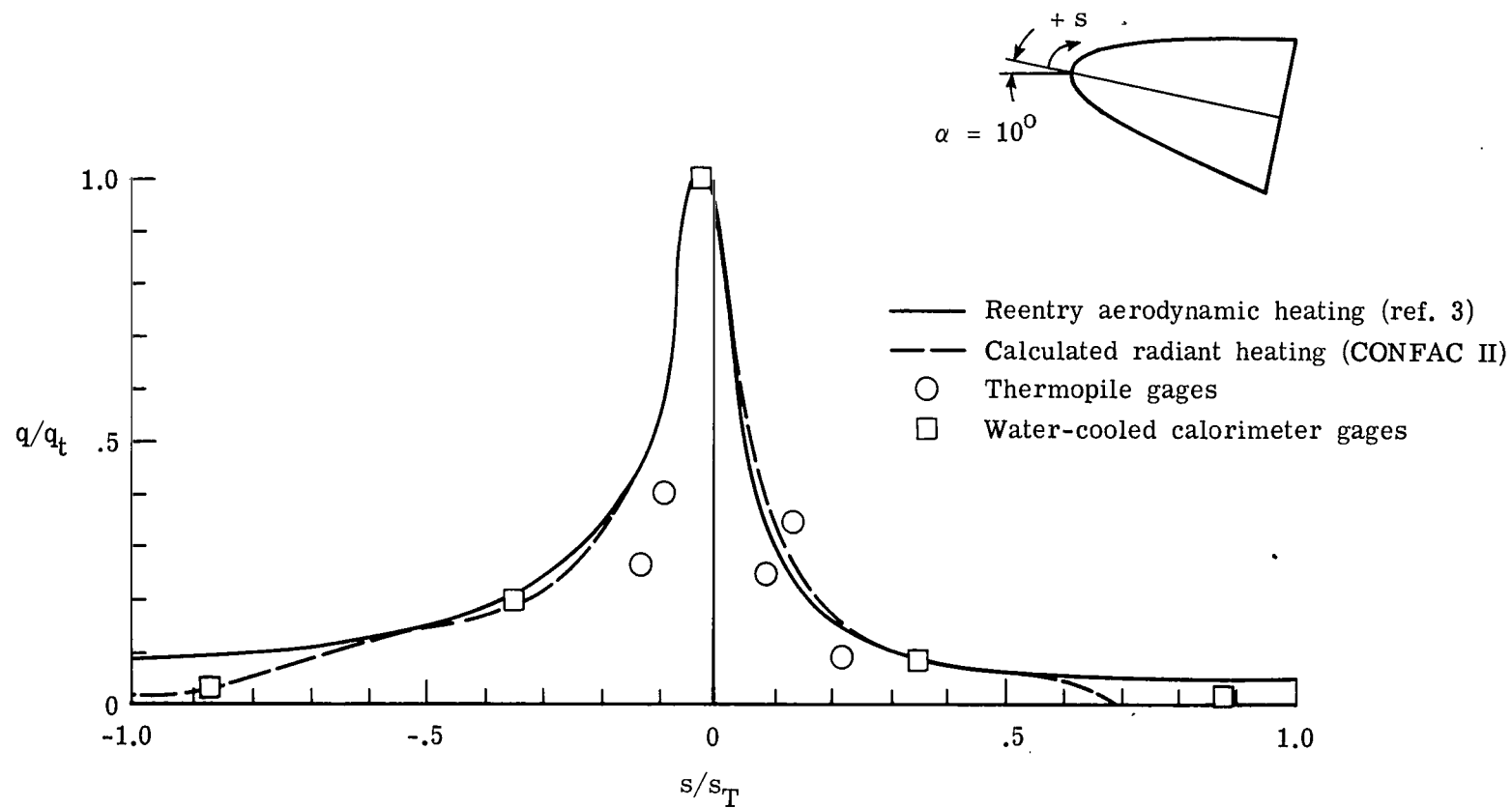
Figure 4.- Normalized cold-wall heating distribution for 10° angle of attack (test 7).
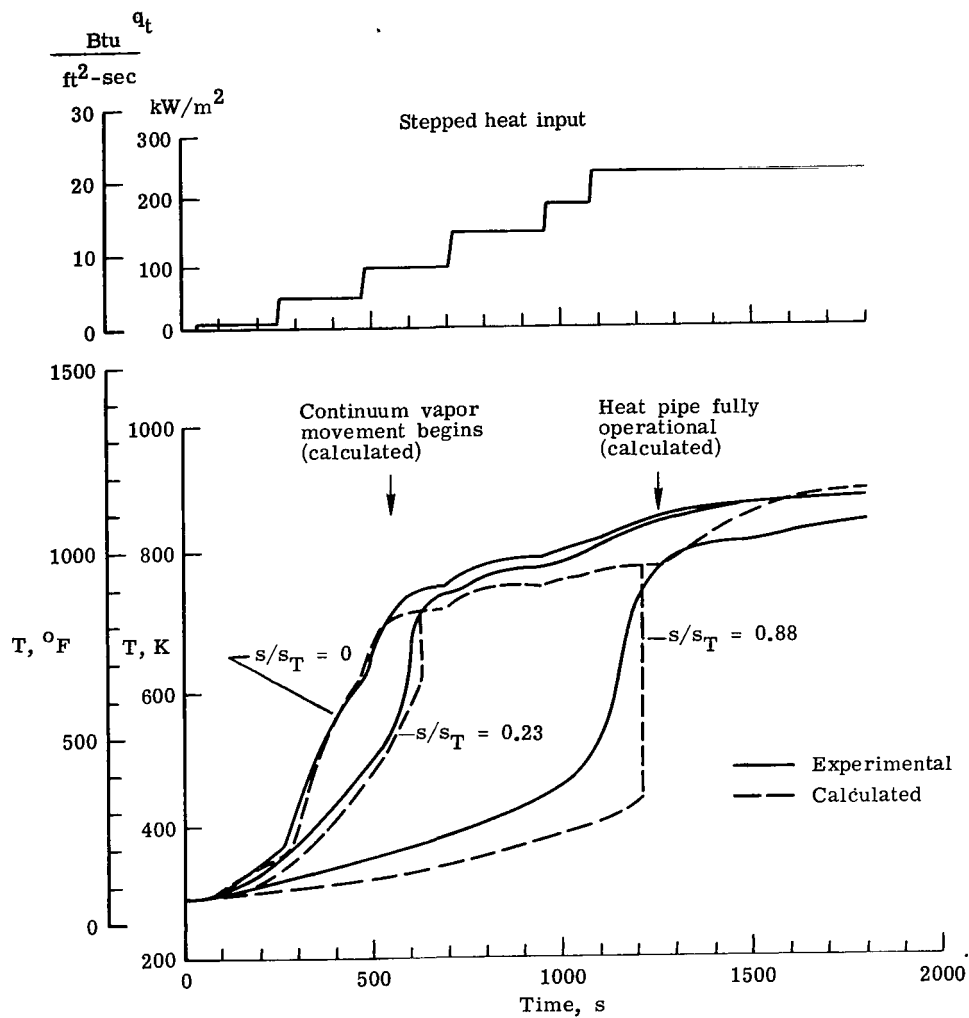
Figure 5.- Temperature history of leading-edge model at s/s_T = 0.0, 0.23, and 0.88 (test 1).
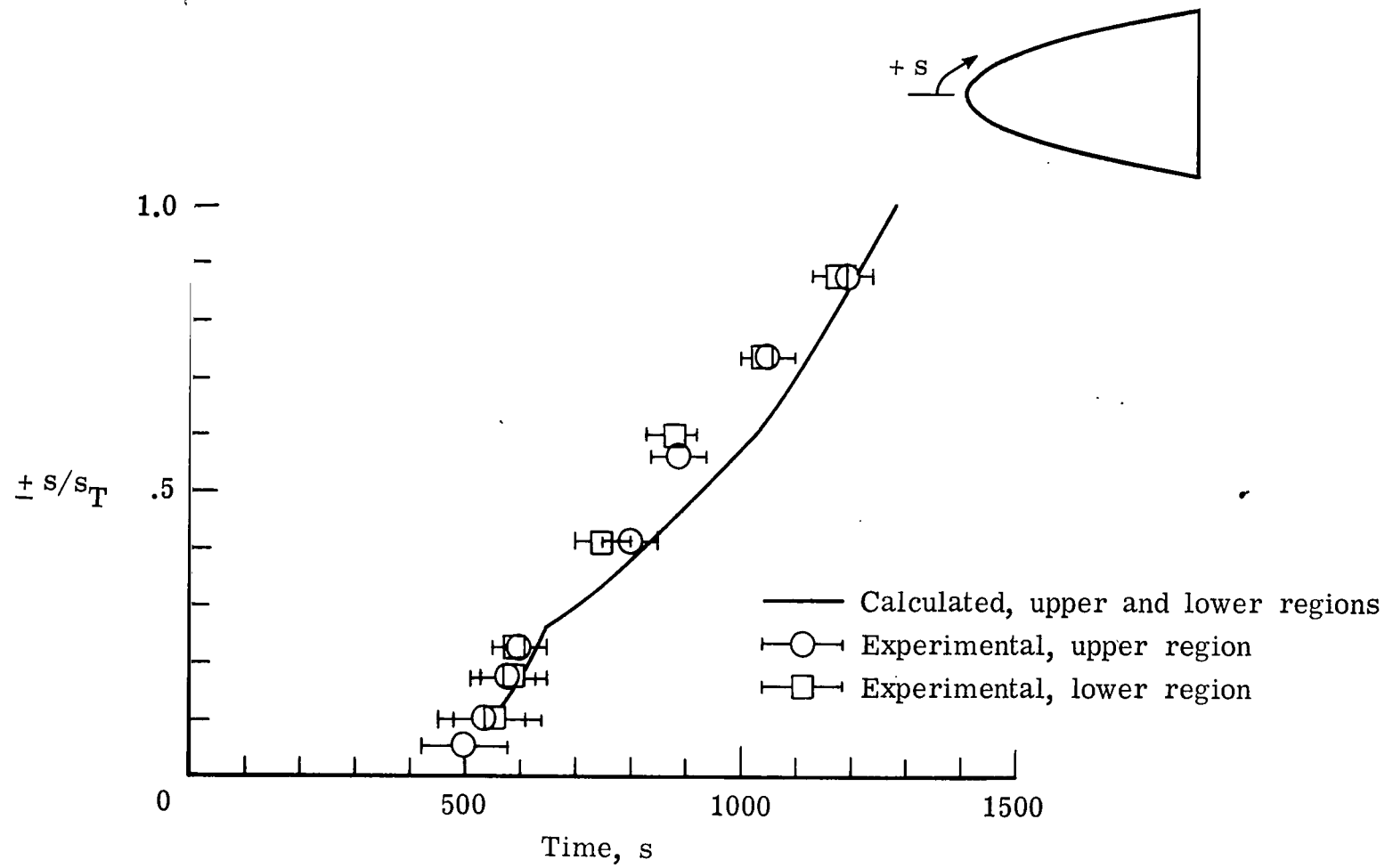
Figure 6.- Heat pipe continuum region growth. $\alpha = 0^\circ$; $s_T = 58.4$ cm; test 1.
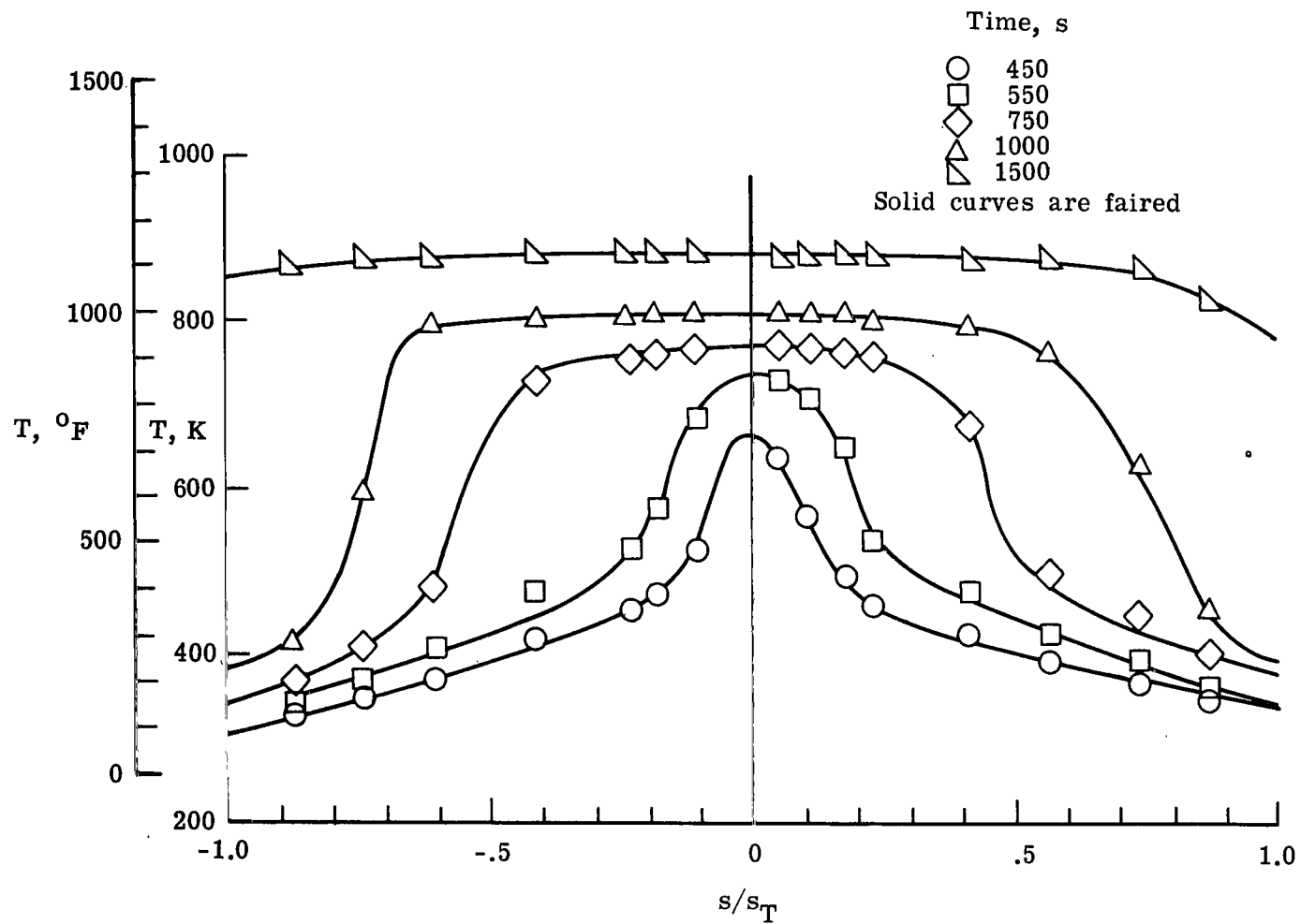
Figure 7.- Experimental heat pipe temperature distributions (test 1).
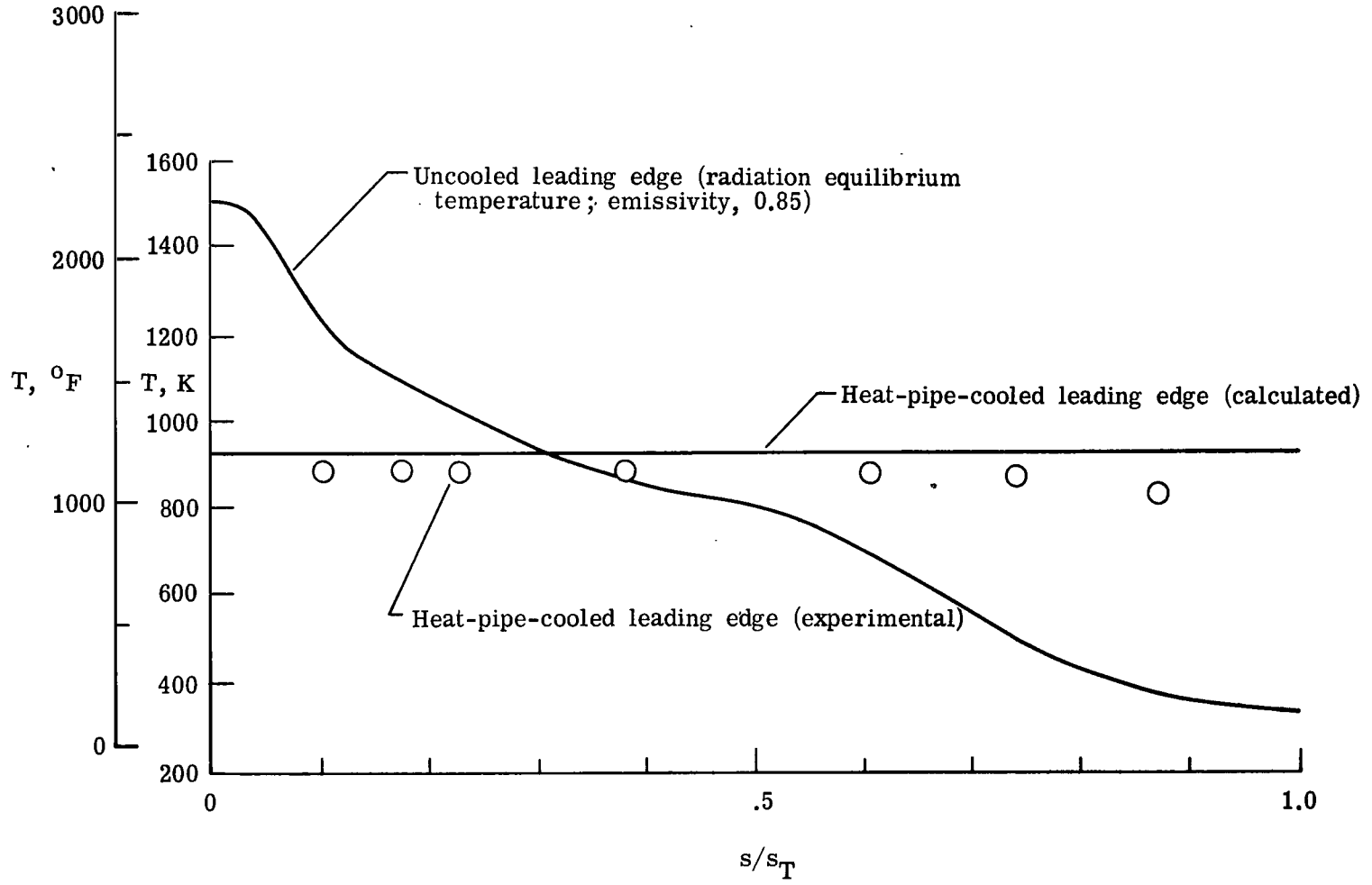
Figure 8.- Uncooled and heat-pipe-cooled leading edge. Test 1; t = 1500 s.
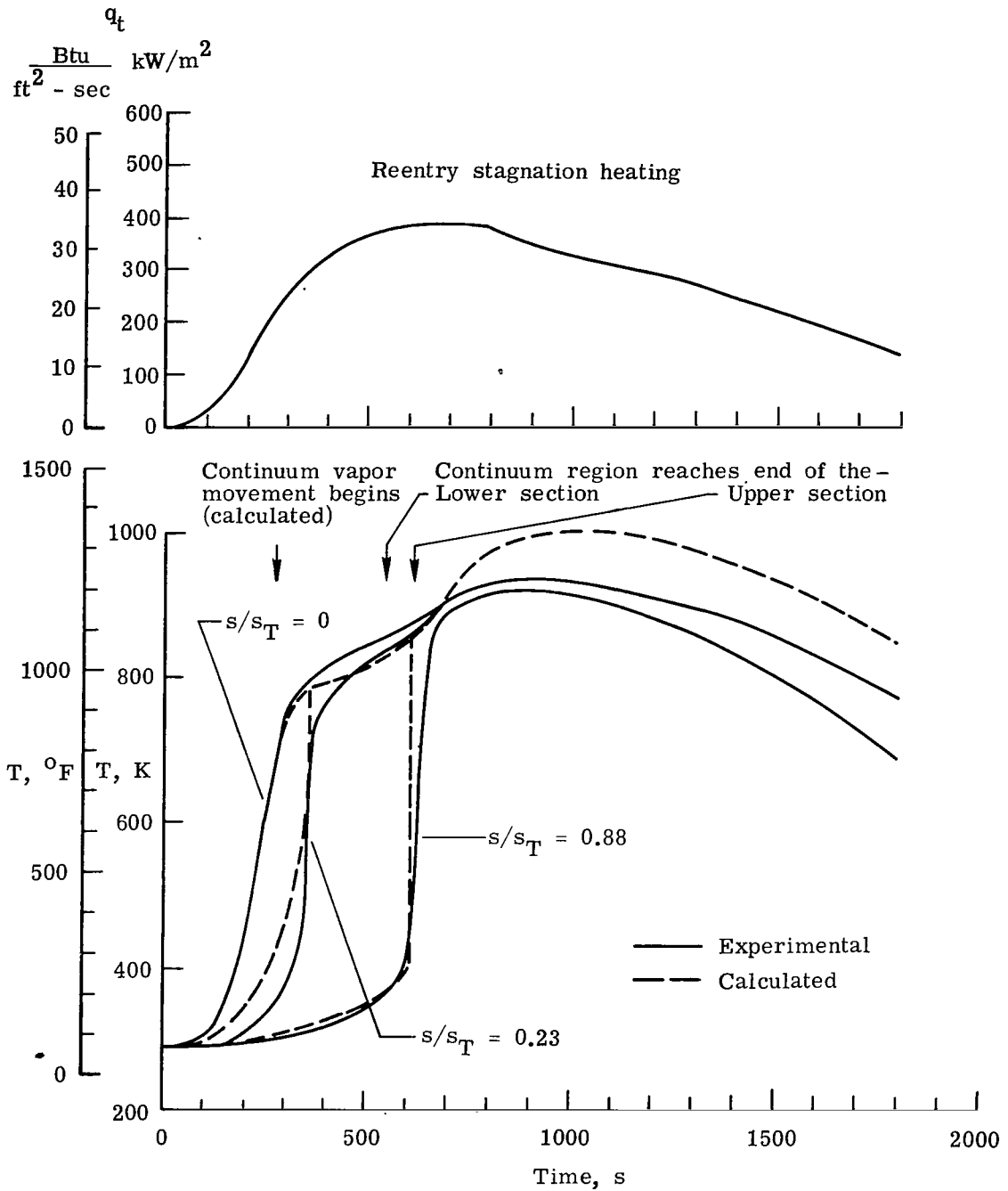
Figure 9.- Temperature history of leading-edge model at
s/s$_T$ = 0.0, 0.23, and 0.88 (test 7).
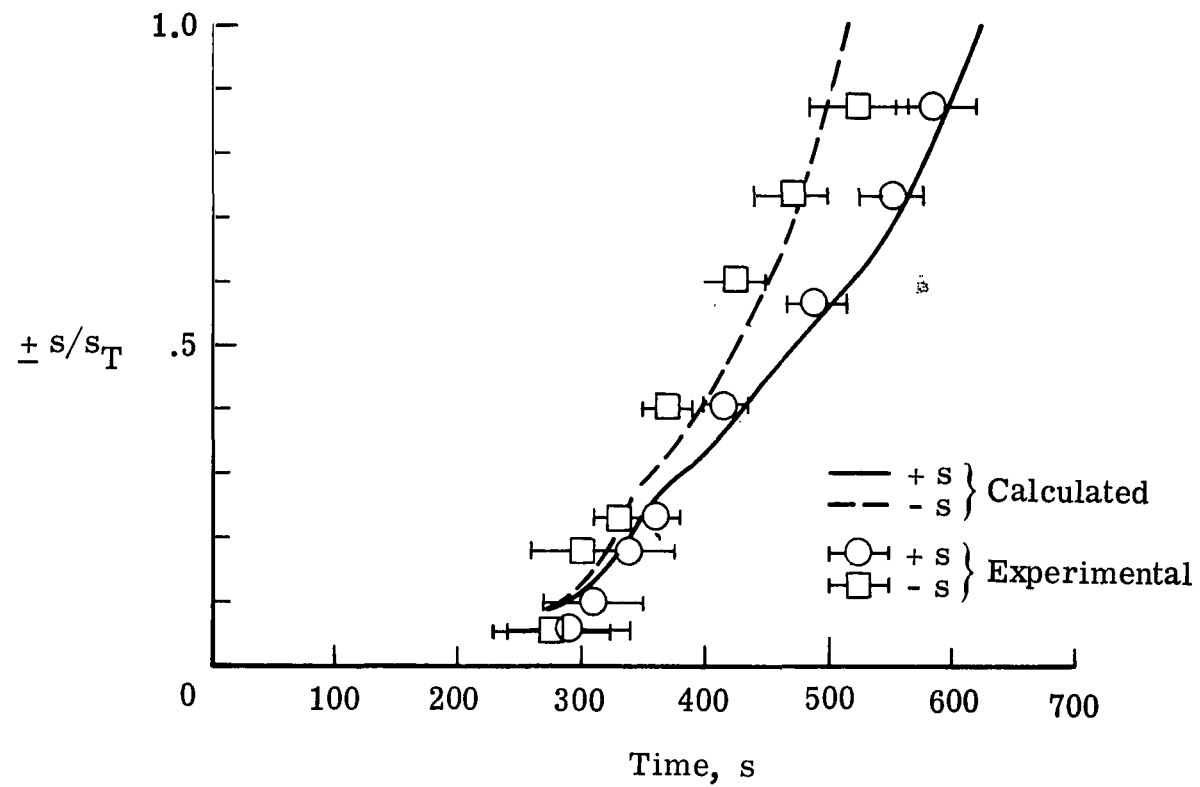
Figure 10.- Heat pipe continuum region growth (reentry simulation test).
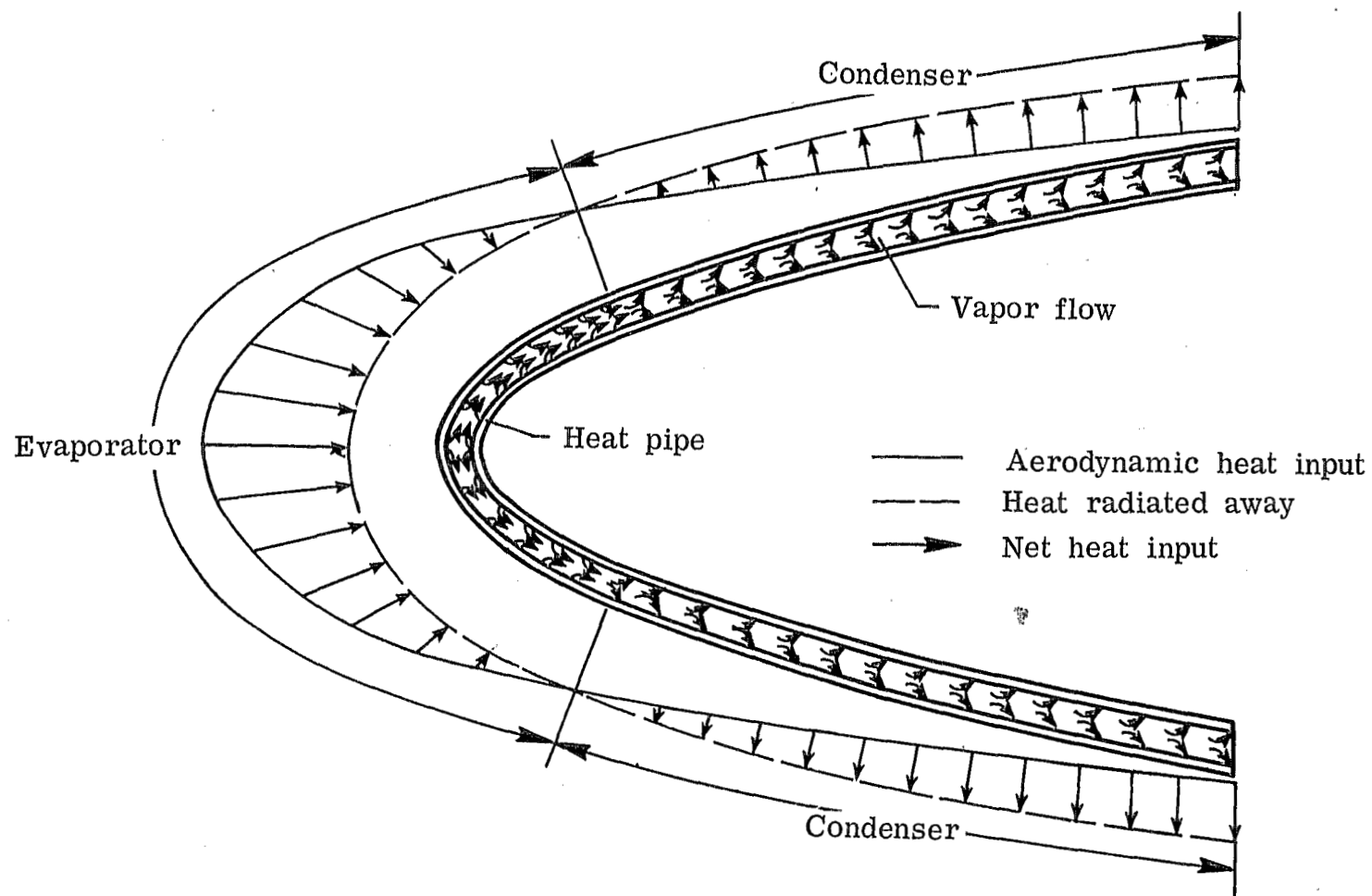
Figure 11.- Schematic diagram of redistribution of heat energy
with a heat-pipe-cooled leading edge.
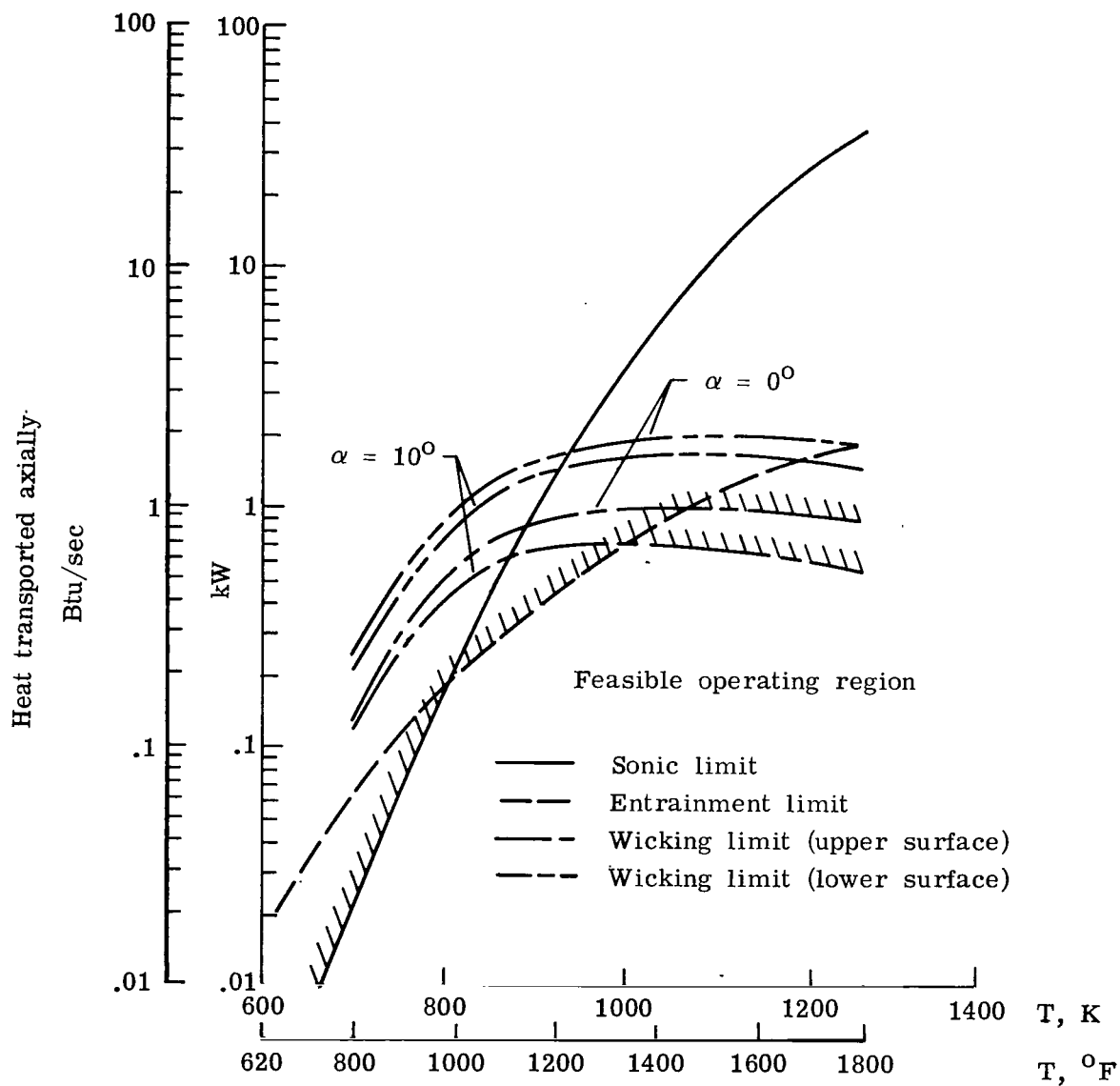
Figure 12.- Heat-transfer performance of heat-pipe-cooled leading edge at angles of attack of 0° and 10°.
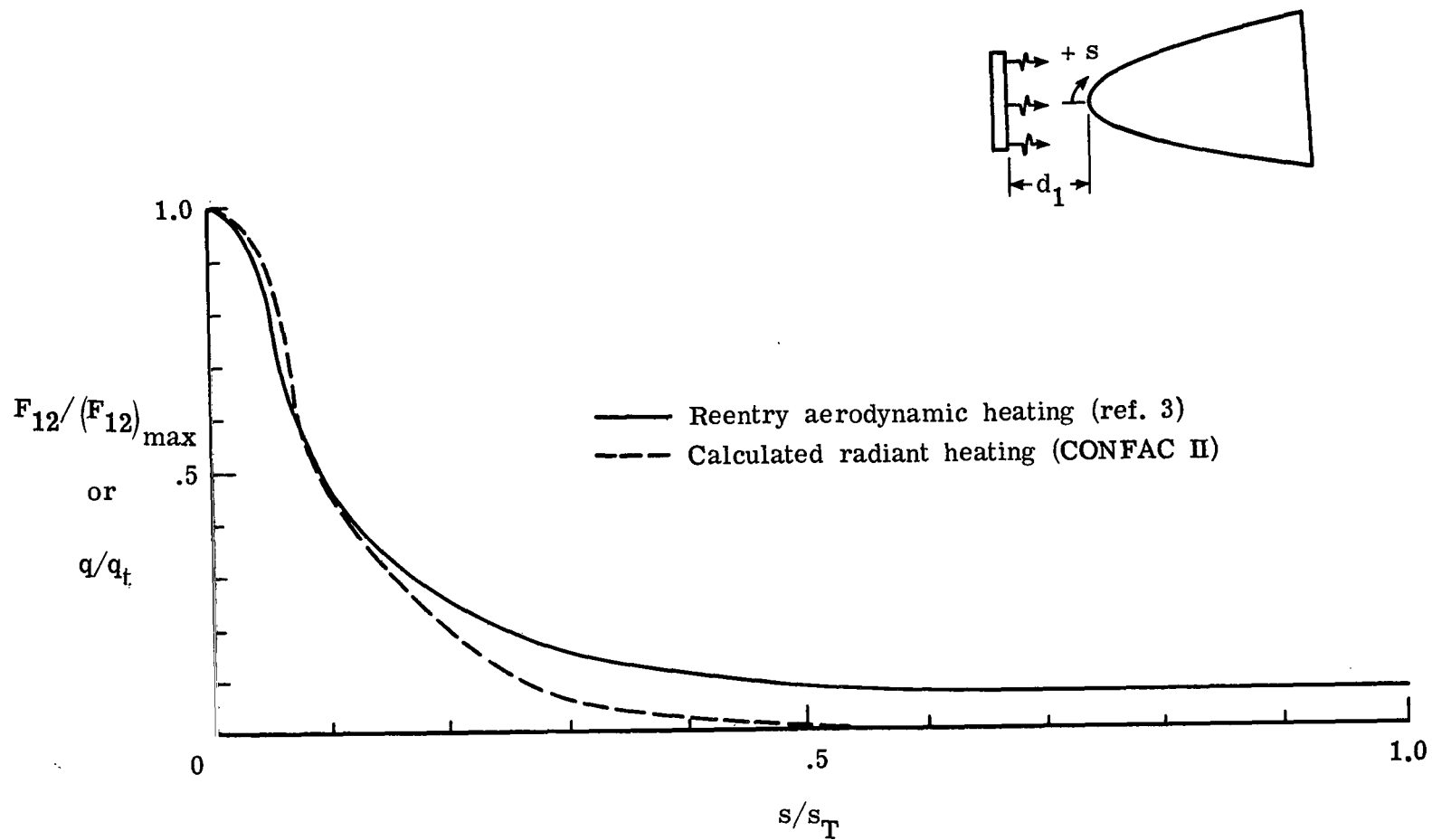
Figure 13.- Aerodynamic and calculated (radiant heater) heating distribution.
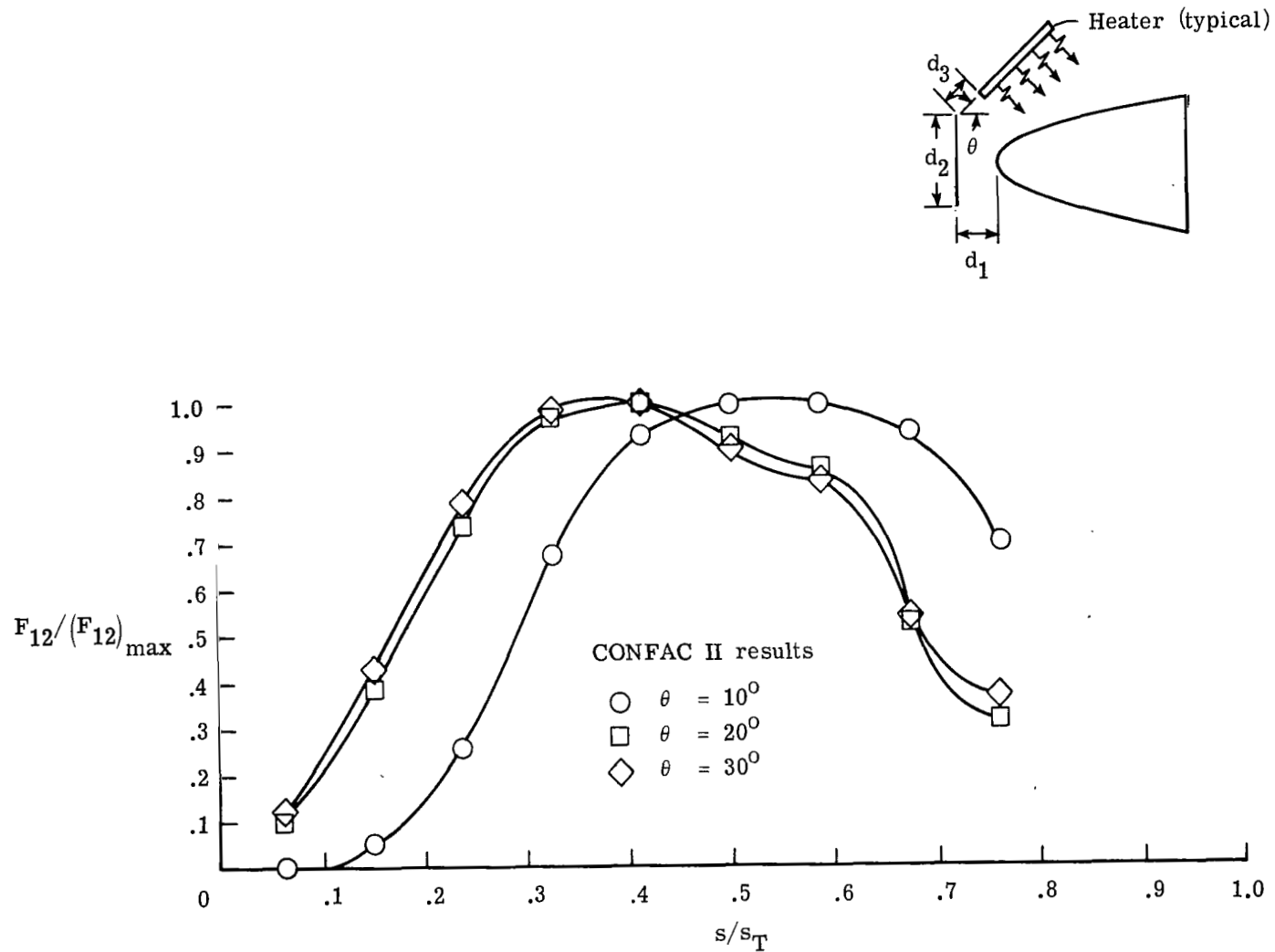Single heater; $\alpha = 0^O$; $d_1 = 2.54$ cm (1 in.).

Figure 14.- Normalized form-factor distributions. Single heater, variable
  orientation; d_1 = 2.5 cm (1 in.); d_2 = 30.5 cm (12 in.);
  d_3 = 7.6 cm (3 in.).

Test configurations			
α, deg	θ_u, deg	θ_ℓ, deg	Tests
0	30	30	1, 2, 3
10	20	40	4, 7
20	10	50	5, 6

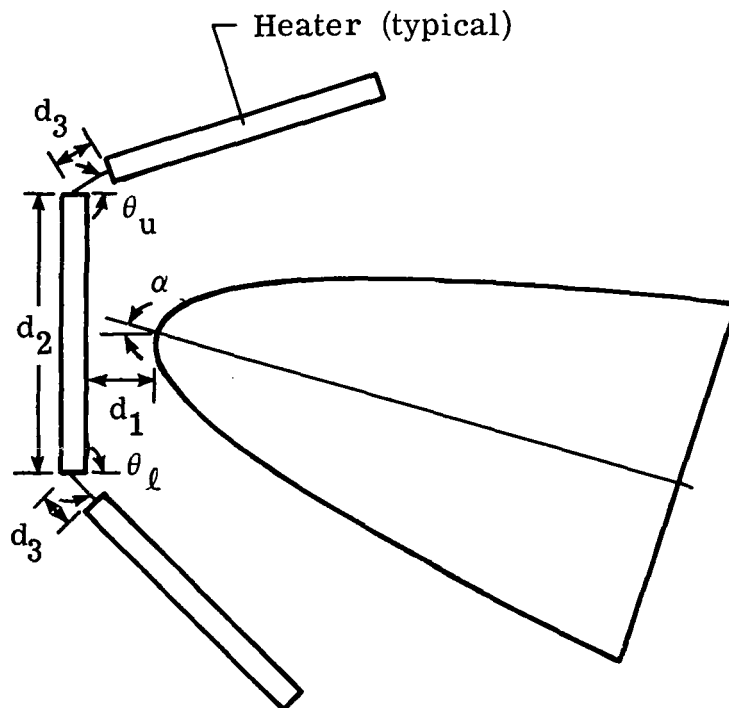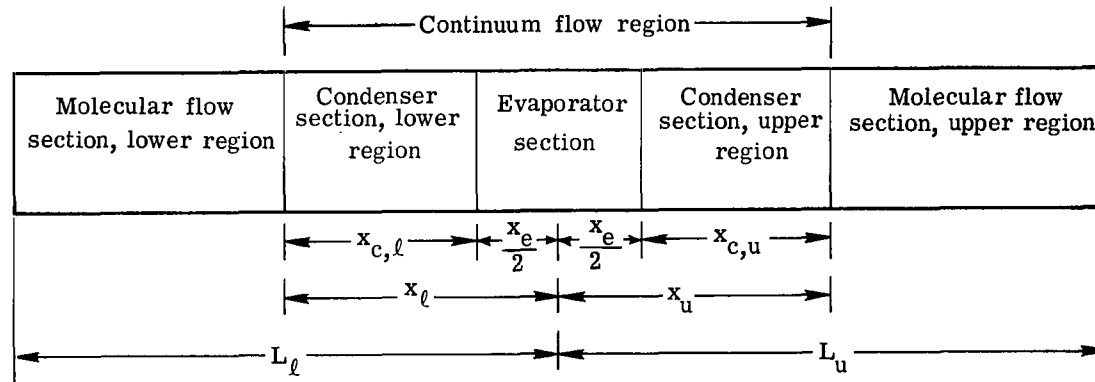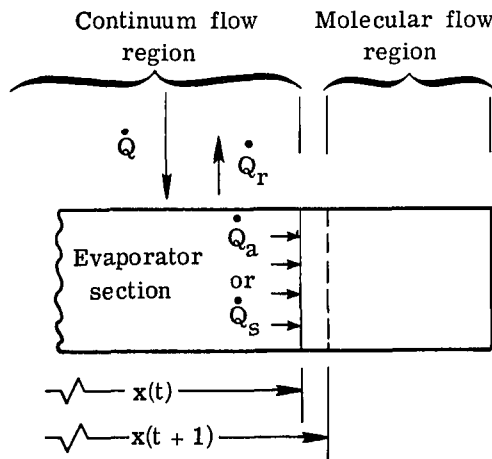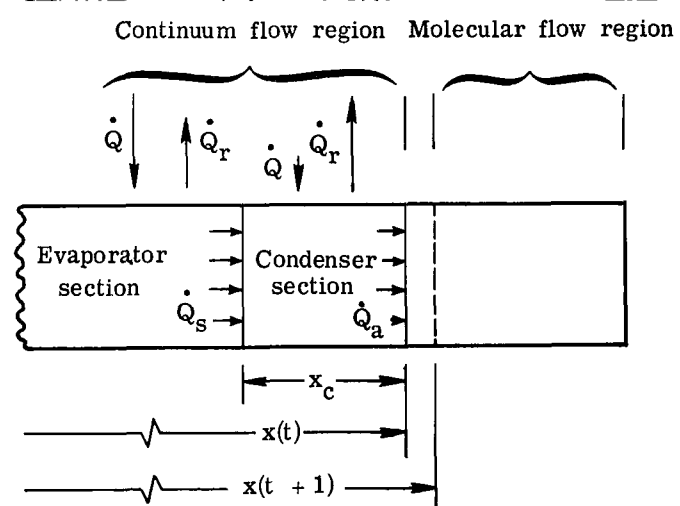| d_1, cm (in.)	d_2, cm (in.)	d_3, cm (in.)
2.54 (1)	30.5 (12)	7.6 (3)

Figure 15.- Schematic diagram of test configurations.

(a) Entire heat pipe with condenser sections propagating
into molecular-flow regions.

(b) Evaporator section propagating
into a molecular flow region.

(c) Condenser section propagating
into a molecular flow region.

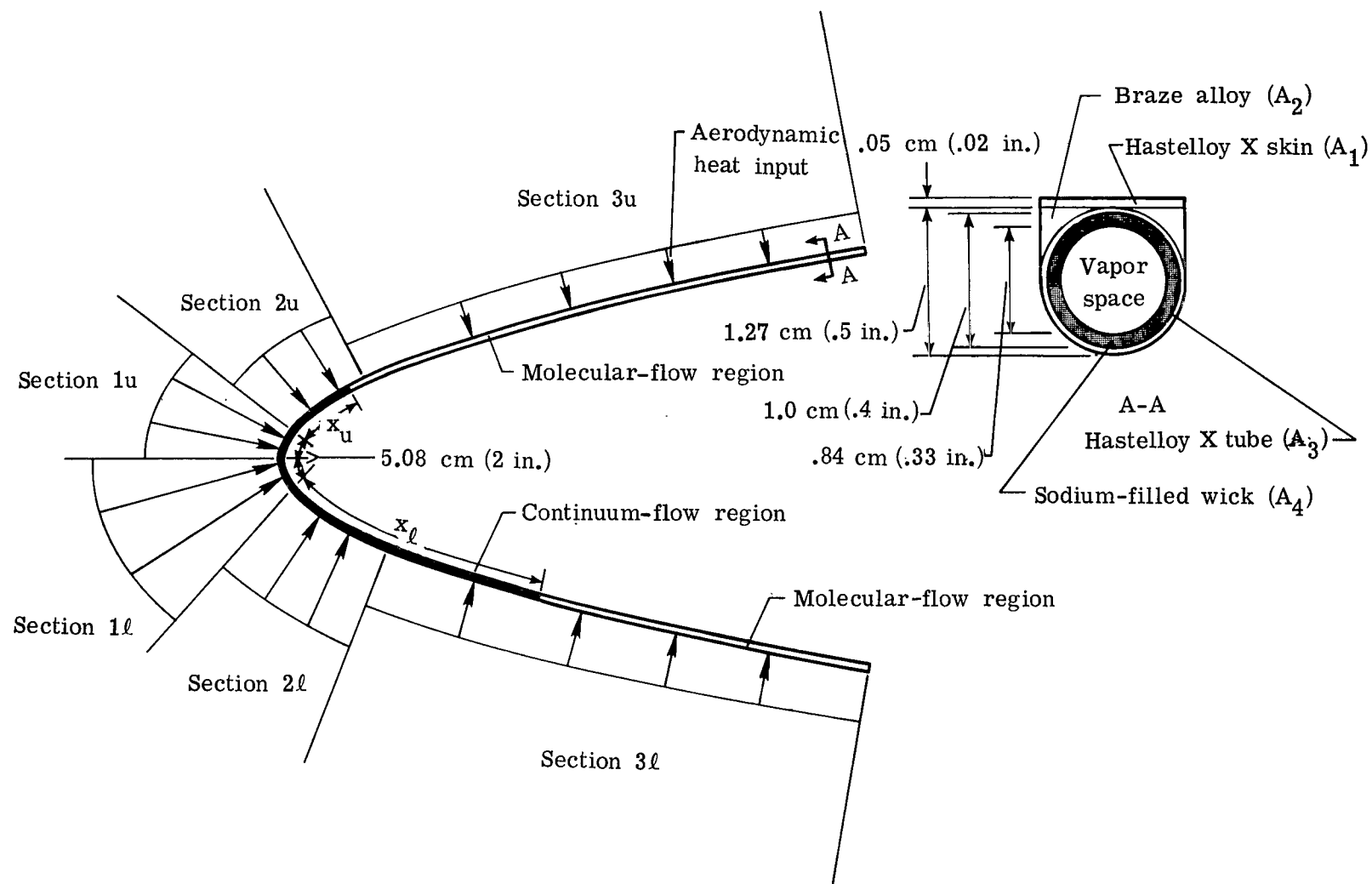Figure 16.- Models used to calculate continuum region temperatures and growth.

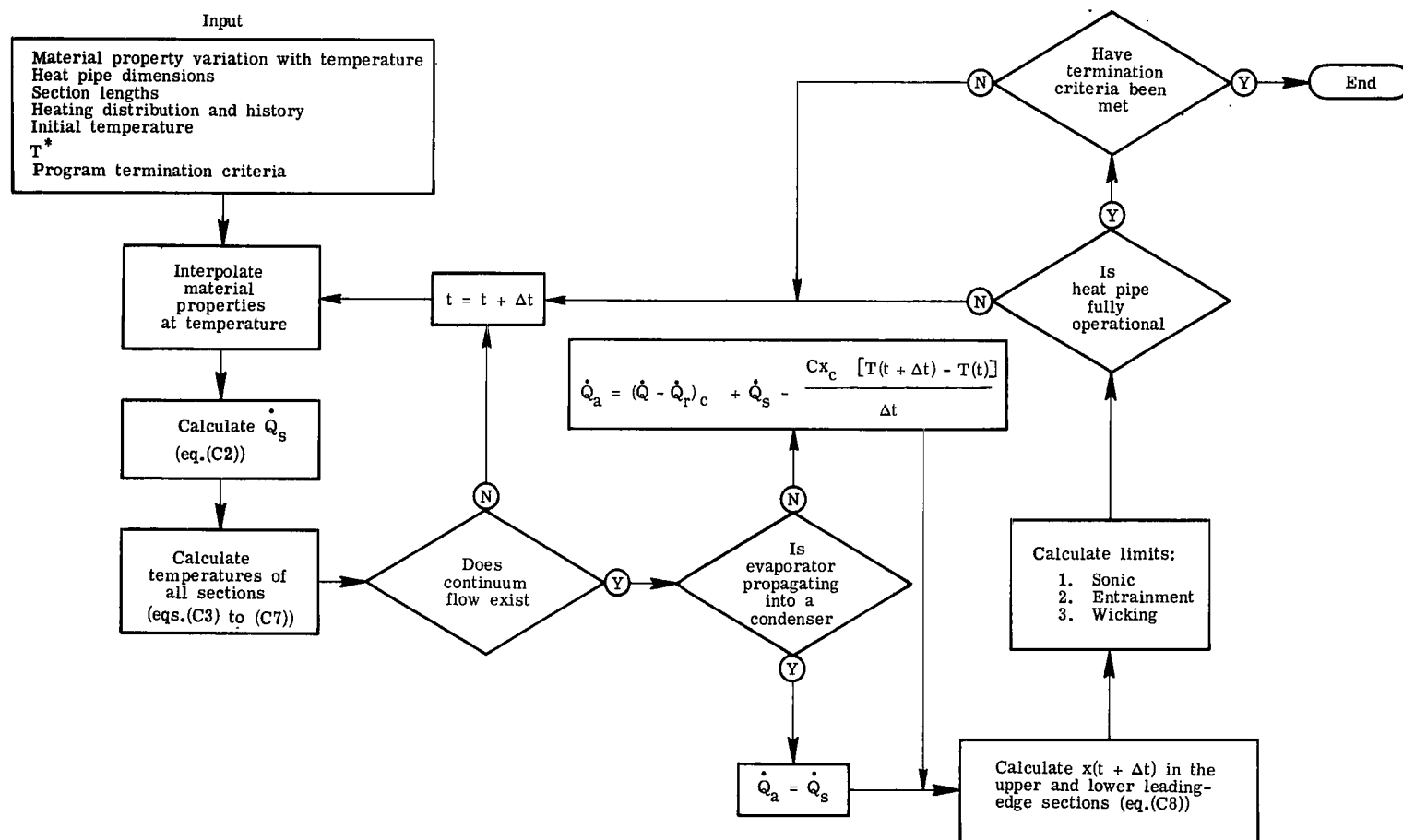Figure 17.- Analysis model of one heat pipe.

Input

Material property variation with temperature
Heat pipe dimensions
Section lengths
Heating distribution and history
Initial temperature
T^*
Program termination criteria

Interpolate material properties at temperature

Calculate $\dot{Q}_s$ (eq.(C2))

Calculate temperatures of all sections (eqs.(C3) to (C7))

Does continuum flow exist

Is evaporator propagating into a condenser

$t = t + \Delta t$

$$\dot{Q}_a = (\dot{Q} - \dot{Q}_r)_c + \dot{Q}_s - \frac{Cx_c \; [T(t + \Delta t) - T(t)]}{\Delta t}$$

$\dot{Q}_a = \dot{Q}_s$

Calculate $x(t + \Delta t)$ in the upper and lower leading-edge sections (eq.(C8))

Calculate limits:
1. Sonic
2. Entrainment
3. Wicking

Is heat pipe fully operational

Have termination criteria been met

End

Figure 18.- Flow diagram of program used to determine heat pipe
thermal behavior.

"The aeronautical and space activities of the United States shall be conducted so as to contribute . . . to the expansion of human knowledge of phenomena in the atmosphere and space. The Administration shall provide for the widest practicable and appropriate dissemination of information concerning its activities and the results thereof."
—NATIONAL AERONAUTICS AND SPACE ACT OF 1958

NASA SCIENTIFIC AND TECHNICAL PUBLICATIONS

TECHNICAL REPORTS: Scientific and technical information considered important, complete, and a lasting contribution to existing knowledge.

TECHNICAL NOTES: Information less broad in scope but nevertheless of importance as a contribution to existing knowledge.

TECHNICAL MEMORANDUMS: Information receiving limited distribution because of preliminary data, security classification, or other reasons. Also includes conference proceedings with either limited or unlimited distribution.

CONTRACTOR REPORTS: Scientific and technical information generated under a NASA contract or grant and considered an important contribution to existing knowledge.

TECHNICAL TRANSLATIONS: Information published in a foreign language considered to merit NASA distribution in English.

SPECIAL PUBLICATIONS: Information derived from or of value to NASA activities. Publications include final reports of major projects, monographs, data compilations, handbooks, sourcebooks, and special bibliographies.

TECHNOLOGY UTILIZATION PUBLICATIONS: Information on technology used by NASA that may be of particular interest in commercial and other non-aerospace applications. Publications include Tech Briefs, Technology Utilization Reports and Technology Surveys.

Details on the availability of these publications may be obtained from:

SCIENTIFIC AND TECHNICAL INFORMATION OFFICE

NATIONAL AERONAUTICS AND SPACE ADMINISTRATION
Washington, D.C. 20546